

# Local isotropy in turbulent boundary layers at high Reynolds number

By SEYED G. SADDOUGHI  
AND SRINIVAS V. VEERAVALLI†

Center for Turbulence Research, Bldg 500, Stanford University, CA 94305, USA and NASA  
Ames Research Center, CA 94035, USA.

(Received 15 June 1993)

To test the local-isotropy predictions of Kolmogorov's (1941) universal equilibrium theory, we have taken hot-wire measurements of the velocity fluctuations in the test-section-ceiling boundary layer of the 80 × 120 foot Full-Scale Aerodynamics Facility at NASA Ames Research Center, the world's largest wind tunnel. The maximum Reynolds numbers based on momentum thickness,  $R_\theta$ , and on Taylor microscale,  $R_\lambda$ , were approximately 370000 and 1450 respectively. These are the largest ever attained in laboratory boundary-layer flows. The boundary layer develops over a rough surface, but the Reynolds-stress profiles agree with canonical data sufficiently well for present purposes. Spectral and structure-function relations for isotropic turbulence were used to test the local-isotropy hypothesis, and our results have established the condition under which local isotropy can be expected.

To within the accuracy of measurement, the shear-stress cospectral density  $E_{12}(k_1)$ , which is the most sensitive indicator of local isotropy, fell to zero at a wavenumber about a decade *larger* than that at which the energy spectra first followed  $-\frac{5}{3}$  power laws. At the highest Reynolds number,  $E_{12}(k_1)$  vanished about one decade *before* the start of the dissipation range, and it remained zero in the dissipation range.

The lower wavenumber limit of locally isotropic behaviour of the shear-stress cospectra is given by  $k_1(\epsilon/S^3)^{\frac{1}{2}} \approx 10$  where  $S$  is the mean shear,  $\partial U/\partial y$ . The current investigation also indicates that for energy spectra this limit may be relaxed to  $k_1(\epsilon/S^3)^{\frac{1}{2}} \approx 3$ ; this is Corrsin's (1958) criterion, with the numerical value obtained from the present data. The existence of an *isotropic* inertial range requires that this wavenumber be much less than the wavenumber at the onset of viscous effects,  $k_1 \eta \ll 1$ , so that the combined condition (Corrsin 1958; Uberoi 1957), is  $S(\nu/\epsilon)^{\frac{1}{2}} \ll 1$ .

Among other detailed results, it was observed that in the dissipation range the energy spectra had a simple exponential decay (Kraichnan 1959) with an exponent prefactor close to the value  $\beta = 5.2$  obtained in direct numerical simulations at low Reynolds number. The inertial-range constant for the three-dimensional spectrum,  $C$ , was estimated to be  $1.5 \pm 0.1$  (Monin & Yaglom 1975). Spectral 'bumps' between the  $-\frac{5}{3}$  inertial range and the dissipative range were observed on all the compensated energy spectra. The shear-stress cospectra rolled-off with a  $-\frac{7}{3}$  power law before the start of local isotropy in the energy spectra, and scaled linearly with  $S$  (Lumley 1967).

In summary, it is shown that one decade of inertial subrange with truly negligible shear-stress cospectral density requires  $S(\nu/\epsilon)^{\frac{1}{2}}$  of not more than about 0.01 (for a shear layer with turbulent kinetic energy production approximately equal to

† Present address: Department of Applied Mechanics, Indian Institute of Technology, New Delhi 110016, India.

dissipation, a microscale Reynolds number of about 1500). For practical purposes many of the results of the hypothesis may be relied on at somewhat lower Reynolds numbers.

## 1. Introduction

The local-isotropy hypothesis, which states that at sufficiently high Reynolds numbers the small-scale structures of turbulent motions are independent of large-scale structures and the mean deformation rate (Kolmogorov 1941, 1962), has been used in most approaches to understanding turbulence, be they theoretical, modelling, or computational methods like large-eddy simulation. The importance of Kolmogorov's ideas arises from the fact that they create a foundation for turbulence theory by defining the nature of the singular limit of vanishing viscosity.

Basically two methods – experiment and direct numerical simulation (DNS) – have been employed to study the statistical properties of the small scales of turbulence. The most powerful present-day computers permit DNS of shear flows only at low Reynolds numbers. Since the high-Reynolds-number requirement is an intrinsic part of the local-isotropy hypothesis, experiments appear to be the only way to investigate this concept – at least for now. This is not an easy task. To overcome the resolution limitations of present-day instruments, high Reynolds numbers must be achieved under controlled conditions in very large facilities.

This report represents a part of a major experimental study of the concept of local isotropy in shear flows at high Reynolds numbers. Acquisition of reliable small-scale experimental data has been of prime concern. It is hoped that the analysis of these data will enhance our understanding of the local-isotropy hypothesis.

### 1.1. Theoretical background

Local isotropy greatly simplifies the statistics of turbulence. Consider for example the average turbulent energy dissipation rate per unit mass  $\epsilon$ , which is given by (e.g. Hinze 1975, p. 218)

$$\epsilon = \nu \left( \frac{\partial u_i}{\partial x_j} + \frac{\partial u_j}{\partial x_i} \right) \frac{\partial u_j}{\partial x_i}, \quad (1)$$

using tensor notation and summation on repeated indices, where  $\nu$  is the kinematic viscosity. Here we use a Cartesian coordinate system  $x_i = (x, y, z)$  with  $x$ -axis along the flow direction,  $y$ -axis normal to the solid surface and  $z$ -axis in the spanwise direction. The respective mean-velocity components in these directions are  $U_i = (U, V, W)$  and the fluctuating components are  $u_i = (u, v, w)$ . Overbars denote time averages. If the dissipating range of eddy sizes is statistically isotropic, (1) reduces to (Taylor 1935)

$$\epsilon = 15\nu \overline{\left( \frac{\partial u_1}{\partial x_1} \right)^2}. \quad (2)$$

At sufficiently high Reynolds numbers and sufficiently small scale, Kolmogorov's universal equilibrium hypothesis (of which local isotropy is a part) states that

$$E(k) = (\epsilon\nu^5)^{\frac{1}{3}} \Phi(k\eta), \quad (3)$$

where  $E(k)$  is the three-dimensional energy spectrum,  $k$  is the wavenumber magnitude,  $\eta \equiv (\nu^3/\epsilon)^{\frac{1}{4}}$  is the Kolmogorov lengthscale and  $\Phi$  is a dimensionless universal function of the non-dimensional wavenumber  $k\eta$ .

If the motion is isotropic, the transverse spectra  $E_{22}(k_1)$  and  $E_{33}(k_1)$  are uniquely determined by the longitudinal spectrum  $E_{11}(k_1)$  (e.g. Batchelor 1953):

$$E_{22}(k_1) = E_{33}(k_1) = \frac{1}{2} \left( 1 - k_1 \frac{\partial}{\partial k_1} \right) E_{11}(k_1), \quad (4)$$

where  $k_1$  is the longitudinal wavenumber and the components of spectra satisfy

$$\int_0^\infty E_{11}(k_1) dk_1 = \overline{u_1^2}, \quad \int_0^\infty E_{22}(k_1) dk_1 = \overline{u_2^2}, \quad \int_0^\infty E_{33}(k_1) dk_1 = \overline{u_3^2}. \quad (5)$$

In an inertial subrange, where by definition the viscous effects are small, the three-dimensional spectrum takes the form (Kolmogorov 1941)

$$E(k) = C \epsilon^{\frac{2}{3}} k^{-\frac{5}{3}}, \quad (6)$$

and, assuming isotropy, the one-dimensional longitudinal and transverse spectra are

$$E_{11}(k_1) = C_1 \epsilon^{\frac{2}{3}} k_1^{-\frac{5}{3}} \quad (7)$$

and

$$E_{22}(k_1) = E_{33}(k_1) = C'_1 \epsilon^{\frac{2}{3}} k_1^{-\frac{5}{3}} \quad (8)$$

respectively. The Kolmogorov constant  $C$  is equal to  $\frac{55}{18} C_1$  (Monin & Yaglom 1975), and (4) evaluated in the inertial subrange gives  $C'_1/C_1 = 4/3$ .

In isotropic flow the shear-stress cospectrum,  $E_{12}(k_1)$ , which satisfies

$$\int_0^\infty E_{12}(k_1) dk_1 = -\overline{u_1 u_2}, \quad (9)$$

is equal to zero. This indicates that for local isotropy the correlation-coefficient spectrum,

$$R_{12}(k_1) \equiv \frac{-E_{12}(k_1)}{[E_{11}(k_1) E_{22}(k_1)]^{\frac{1}{2}}}, \quad (10)$$

should fall to zero at high wavenumbers. Also, the spectral coherency, or cross-spectrum modulus, defined by

$$H_{12}(k_1) \equiv \frac{E_{12}^2(k_1) + Q_{12}^2(k_1)}{E_{11}(k_1) E_{22}(k_1)}, \quad (11)$$

where  $Q_{12}(k_1)$  is the quadrature spectrum (see e.g. Bendat & Piersol 1986), is zero in an isotropic flow.

Kolmogorov (1941) proposed scaling laws in the inertial subrange for structure functions, which are moments of the velocity differences evaluated at points separated by distances  $r$  (for the present study  $r$  corresponds to longitudinal distances). The second-order longitudinal and transverse structure functions are given by

$$D_{11}(r) \equiv \overline{[u_1(x_1+r) - u_1(x_1)]^2} = C_2 \epsilon^{\frac{2}{3}} r^{\frac{2}{3}} \quad (12)$$

and

$$D_{33}(r) = D_{22}(r) \equiv \overline{[u_2(x_1+r) - u_2(x_1)]^2} = C'_2 \epsilon^{\frac{2}{3}} r^{\frac{2}{3}} \quad (13)$$

respectively in isotropic flow, where  $C_2 \approx 4C_1$  (Monin & Yaglom 1975) and  $C'_2/C_2 = 4/3$ . This structure-function behaviour is also known as 'Kolmogorov's  $\frac{2}{3}$  law'.

The third-order longitudinal structure function for homogeneous isotropic turbulence was derived from the Navier–Stokes equations by Kolmogorov, without any appeal to self-similarity (Landau & Lifshitz 1987, p. 140). In the inertial subrange ( $r \gg \eta$  and the viscous effects are small) this takes the form

$$D_{111}(r) \equiv \overline{[u_1(x_1+r) - u_1(x_1)]^3} = -\frac{4}{5}\epsilon r. \quad (14)$$

Note that there is no arbitrary constant in this equation, which provides an easy way to estimate the dissipation in an isotropic flow.

The above relations can be used to experimentally investigate the concept of local isotropy. The accuracy to which these relations are satisfied in a given flow is a measure of the accuracy of the local-isotropy hypothesis.

### 1.2. A brief review of previous work

Since Kolmogorov proposed his theory, there have been many experiments, conducted in wakes, jets, mixing layers, a tidal channel, and atmospheric and laboratory boundary layers, in which attempts have been made to verify – or refute – the local-isotropy hypothesis. However, a review of the literature over the last five decades indicates that, despite all these experiments in shear flows, there is no consensus in the scientific community regarding this hypothesis. Excellent reviews of this situation already exist. Examples include the articles in the *Proceedings of the Royal Society*, dedicated to the 50th anniversary of Kolmogorov's ideas (Hunter, Phillips & Williams 1991) (in particular those by Van Atta 1991 and Sreenivasan 1991, which directly address the concept of local isotropy). See also the reviews by Champagne (1978), Mestayer (1982) and Browne, Antonia & Shah (1987). To show the extent of disagreement, conclusions from a few experiments and recent theoretical and computational studies will be cited here.

One of the earliest studies was by Townsend (1948), whose measurements of  $\overline{(\partial u_1/\partial x_1)^2}$ ,  $\overline{(\partial u_2/\partial x_1)^2}$  and  $\overline{(\partial u_3/\partial x_1)^2}$  in the wake of a cylinder confirmed local isotropy. However, Browne *et al.* (1987) measured the nine mean-square velocity derivatives in (1) in the wake of a cylinder at low  $R_\lambda$  ( $\approx 40$  to 80), and found that local isotropy was not satisfied in the dissipation range.

Uberoi (1957) found that the mean-square vorticity fluctuations measured in a boundary layer did not satisfy the local-isotropy hypothesis, but Mestayer (1982), who presented  $u$ - and  $v$ -spectra (no  $w$ -spectrum was measured) for only one position ( $y/\delta = 0.33$ ) in a boundary layer at  $R_\lambda \approx 616$ , concluded that the local-isotropy criterion was satisfied in the dissipation range but not in the inertial subrange. Mestayer had to use Wyngaard's (1968) correction for his spectra, because the hot-wire spatial resolution was poor; the hot-wire length was 4.5 times greater than Kolmogorov lengthscale, which resulted in the attenuation of the high-wavenumber part of the spectra.

Grant, Steward & Moilliet (1962) and Grant & Moilliet (1962) showed that spectra of both the streamwise and a cross-stream components of turbulence in a tidal channel at high Reynolds numbers displayed more than two decades of  $-\frac{5}{3}$  power law. In contrast, Karyakin, Kuznetsov & Praskovsky (1991) concluded that, in a return channel of a wind tunnel ( $R_\lambda \approx 3000$ ), neither the inertial subrange nor the dissipative range were isotropic. Karyakin *et al.* used only X-wires to measure the longitudinal and transverse components of spectra. Wyngaard (1968) strongly recommends that measurements of the longitudinal spectrum should be taken with a single wire, because the crosstalk associated with X-wires attenuates the high-wavenumber part of the longitudinal spectrum much more significantly than the transverse spectra. This effect

results in a spurious anisotropy, as further emphasized by the recent study of Ewing & George (1992).

There have recently been a number of theoretical and computational studies stressing the importance of *non-local* (in Fourier space) interactions in the energy cascade process, and this brings into question Kolmogorov's concept of a *local* self-similar cascade. Domaradzki & Rogallo (1988) and Domaradzki, Rogallo & Wray (1990) showed that the energy transfer between similar small scales is largest when the third leg of the triad is a large scale. Yeung & Brasseur (1991) and Brasseur (1991) also demonstrated the importance of non-local transfer in their numerical simulations and argued that such interactions are important even in the high-Reynolds-number limit. However, Waleffe (1991) showed that if one considers all possible non-local triads, the net local transfer due to non-local interactions is not significant, thus local isotropy may not be affected by large-scale anisotropy or mean strain.

Batchelor (1946) introduced the theory of local axisymmetry – invariance with respect to rotation about a preferred direction – which was later extended by Chandrasekhar (1950). Recently, George & Hussein (1991) and Antonia, Kim & Browne (1991) have proposed that in shear flows the local-isotropy assumption should be relaxed to one of local axisymmetry about the streamwise direction and showed that the derivative moments obtained by experiment and by direct numerical simulation in low-Reynolds-number flows supported the local-axisymmetry assumption.

In simple shear flows, where the basic strain rate is  $S = \partial U / \partial y$ , the non-dimensional shear-rate parameter

$$S^* \equiv Sq^2/\epsilon, \quad (15)$$

which is the ratio of the large-eddy timescale ( $q^2/\epsilon$ ) to the timescale of mean deformation ( $S^{-1}$ ), characterizes the effects of mean-strain rate on the energy-containing turbulence scales (Moin 1990; Lee, Kim & Moin 1990): here  $q^2 (\equiv \overline{u_i u_i})$  is twice the turbulent kinetic energy per unit mass. The shear-rate parameter in a simulated turbulent channel flow (Lee *et al.* 1990), reached a maximum value of about 35 at  $y^+ \approx 10$  ( $y^+ \equiv yU_\tau/\nu$ , where  $U_\tau$  is the wall-friction velocity) in the viscous sublayer and decreased to a value of about 6 for  $y^+ > 50$ . Durbin & Speziale (1991) examined the equation for the dissipation-rate tensor and showed that *exact* local isotropy is inconsistent with the presence of mean-strain rate.

On the other hand, Corrsin (1958) proposed that local isotropy may exist in shear flows in the 'mixed range' of spectra (the wavenumber range where both inertial transfer and viscous dissipation are important and where most of the dissipation occurs), when the ratio of the Kolmogorov to mean-shear timescales

$$S_c^* \equiv S(\nu/\epsilon)^{\frac{1}{2}} \ll 1. \quad (16)$$

Note that, for a shear layer with (shear) production of turbulent kinetic energy approximately equal to dissipation,  $S_c^* \sim (R_\lambda)^{-1}$  approximately. Uberoi (1957) argued that, since in wall-bounded flows most of the production and dissipation take place near the wall, where they depend only on  $y^+$  and are independent of bulk Reynolds number,  $S_c^*$  should also be independent of Reynolds number and will have a constant value: in the log-layer  $S_c^* \sim (y^+)^{-\frac{1}{2}}$ . Uberoi also argued that in free-shear flows, such as jets, the situation is quite different and  $S_c^*$  is a function of  $(R_\delta)^{-\frac{1}{2}}$ , where  $R_\delta$  is the Reynolds number based on the half-width of the jet.

Using the channel-flow DNS data at low Reynolds number, Antonia & Kim (1992) found  $S_c^*$  to have a constant value of about 2.5 in the viscous sublayer and a reduction to a very small values for  $y^+ > 60$ . Antonia & Kim stated that  $S_c^*$  is better behaved than  $S^*$  because at the wall, where  $S$  is largest,  $S_c^*$  has a constant value, whereas  $S^*$  goes to

zero. They also suggested that the Corrsin–Uberoi criterion is too restrictive and may be relaxed to  $S_c^* \leq 0.2$  for the small scales to be isotropic.

### 1.3. Objectives of the present investigation

An experiment to investigate the local-isotropy hypothesis in simple shear flows has to satisfy certain conditions. These are examined below.

It is imperative that the Reynolds number of the flow be high enough to separate the dissipating eddies sufficiently from the energy-containing scales. Most of the previous laboratory experiments do not satisfy this requirement. We do need to know the large-scale parameters governing the development of the shear flow. These are rather difficult to determine if the measurements are obtained in an uncontrolled environment. To identify the parameters (e.g.  $S$ ,  $S_c^*$ ) governing the degree of anisotropy of the small scales, it is important that the measurements be conducted at a variety of Reynolds numbers and/or basic mean-strain rates, to cover a range of  $S_c^*$ .

Spatial-resolution problems, which arise because hot wires can resolve only those eddies that have lengthscales the same or larger than the hot-wire length, have affected most of the previous studies. It has been shown that accurate measurements can be obtained with hot wires having (active) length-to-diameter ratios of about 200 (see e.g. Perry 1982; Ligrani & Bradshaw 1987). Very short wires must be extremely thin to satisfy this criterion, and the separation between the sensors in an X-wire must also be reduced, which in effect increases the crosstalk (and these will be accompanied by a lot of other problems, such as manufacturing and operational difficulties). The only practical option is to use large facilities where (i) high Reynolds numbers can be achieved and (ii) Kolmogorov scales can be resolved by standard hot wires. Furthermore,  $u_1$ -spectra should be measured only by single wires to avoid the severe attenuation at the high wavenumbers due to X-wire crosstalk. (Other instrumentation requirements will be discussed in §2.)

In experimental work, Taylor's hypothesis is used to deduce wavenumber spectra from frequency spectra. For small-scale measurements, particularly those in the dissipation range, this hypothesis can be used accurately only in flows where the local turbulence intensity ( $\overline{u_1^{2\frac{1}{2}}}/U$ ) is less than 0.1. Lumley (1965) and Wyngaard & Clifford (1977) estimate that at the highest wavenumbers the errors in the longitudinal and transverse spectra will then be less than 5% and 3% respectively.

The objective of the present study is to investigate the local-isotropy hypothesis in a shear flow by conducting a fresh experiment that adheres to all the requirements listed above. However, it may be noted that in experimental work it is only possible to concentrate on a few measures of isotropy, where undoubtedly some are satisfied before others. Therefore, we cannot be certain whether a state of *full* local isotropy is obtained.

## 2. Experimental facilities and techniques

The experiments described here were conducted in the boundary layer on the test-section ceiling of the Full-Scale Aerodynamics Facility – commonly referred to as the 80 × 120 foot wind tunnel – at NASA Ames Research Center. The test section is approximately 24.4 m high, 36.6 m wide, and more than 50 m long, which makes it the largest wind tunnel in the world. The measurement station was located towards the end of the test section on the centreline of the tunnel ceiling. The data recording equipment and a small wind tunnel used for calibrating the hot wires were installed in the attic above the test-section ceiling. The present measurements were performed in an empty

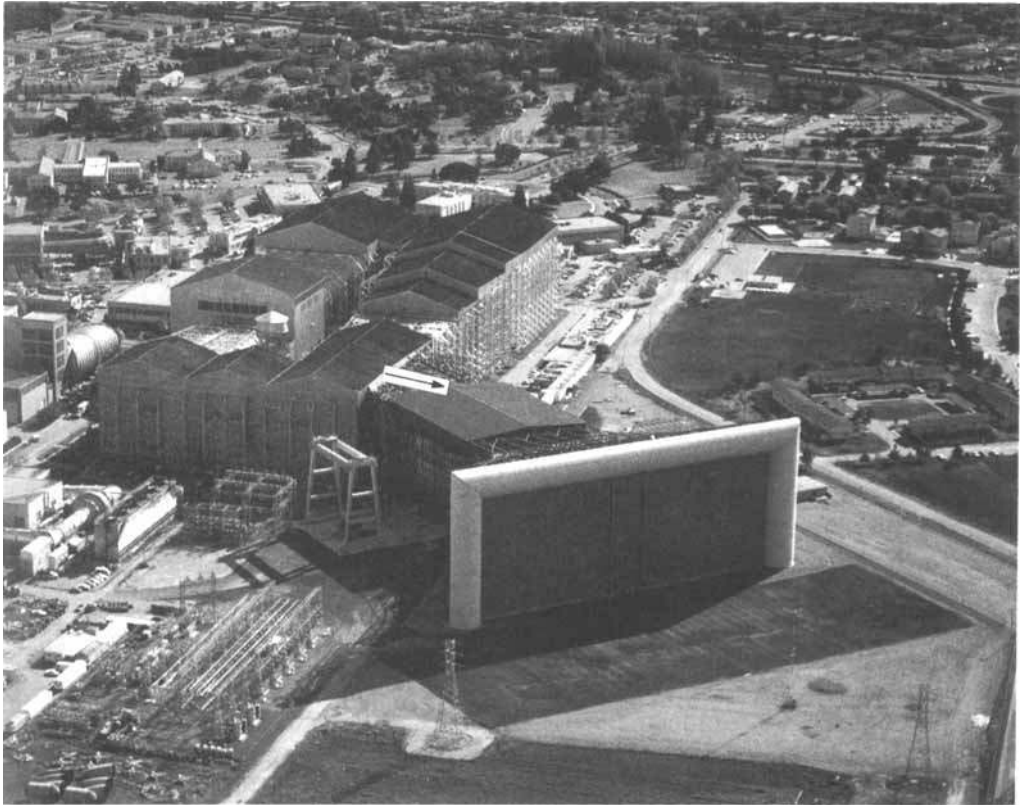


FIGURE 1. An aerial view of the Full-Scale Aerodynamics Facility at NASA Ames Research Center, showing the intake to the  $80 \times 120$  foot test section. The arrow shows our measurement location in the attic.

tunnel fully dedicated to our experiments. An aerial view of this wind tunnel (figure 1), which shows the intake to the  $80 \times 120$  foot test section and our measurement location in the attic, illustrates the scale of the experiment.

All four walls of the test section are lined with acoustic panelling (perforated metal plates, having staggered circular holes of diameter approximately 2.5 mm, placed over foam), which produces a rough-wall turbulent boundary layer. These panels, the large-scale longitudinal grooves in the contraction walls, and occasional small protrusions due to the light ports, produced non-canonical flow close to the wall, but, as will be shown later, outside the wall region the Reynolds stresses followed standard zero-pressure-gradient turbulent-boundary-layer behaviour. It is important to emphasize that it is desirable, but not necessary, to investigate the concept of local isotropy in a canonical boundary layer.

### 2.1. Measurement conditions and strategy

During the course of our feasibility studies (Veeravalli & Saddoughi 1991), we found that, owing to the lack of attic ventilation, the temperature in our calibration tunnel was higher than the temperature inside the  $80 \times 120$  foot test section. To obtain a fairly good temperature adjustment for the calibration, the intake of the blower of the calibration tunnel was connected to an air-conditioner via pipes having valves for controlling the intake of cold air. To reduce fluctuations of mean temperature at the exit of the calibration tunnel, the pipe that connected the output of the blower to the

intake of the calibration tunnel was packed with copper wool. The measured mean temperature across the exit of the calibration tunnel was uniform to within 0.1 °C. All measurements were performed between midnight and mid-morning to minimize the difference between the temperature in the attic and that inside the tunnel. The temperature differences between the calibrations and the actual experiments were generally less than 3 °C. In addition, the hot wires were operated with a resistance ratio of 2.0 rather than the usual 1.8 to further reduce the possibility of drift due to temperature changes. To reduce the chances for changes in the hot-wire characteristics and deviations from the calibration, our traverse mechanism was designed such that the same cables and probe holders could be used during both the calibration and actual measurements, without disconnecting the hot wires (see Perry 1982).

In the present experiments we were faced with a limitation of hot-wire anemometry that dictated our measurement strategy. During our feasibility studies, which were conducted at a free-stream velocity of 40 m s<sup>-1</sup>, it was noted that, apart from high-frequency spikes, a rise with frequency in the tail of the spectra occurred before the final roll-off due to the low-pass filter (cut-off set at 100 kHz). This rise, which was proportional to the square of frequency ( $f^2$ ), was of great concern since it occurred at the expected Kolmogorov frequency for that speed. Therefore, we connected all of our electronic equipment to a power conditioner (Oneac CB 1115) and uninterruptible power supply (Clary PC 1.25K), which supplied clean power and prevented loss of data due to possible power failure. These reduced the background electronic noise, but the tails of the spectra were still contaminated by the  $f^2$  behaviour. To isolate the source of this problem, we conducted extensive tests, which included taking spectral measurements at the free stream of our calibration tunnel and in still air at different laboratories with a variety of hot-wire filaments using hot-wire bridges manufactured by different companies. Under all these different experimental conditions, the  $f^2$  behaviour was present in all the spectra (Saddoughi 1992). The conclusion from these tests was that the performance of all the hot-wire bridges at high frequencies was limited by this  $f^2$  noise, and that, at a free-stream velocity of 50 m s<sup>-1</sup> where the Kolmogorov frequency near the mid-layer of the boundary layer was of the order of 60 kHz, this rise in the tail of the spectrum was inevitable.

Our experiments were therefore divided into two sets. First, to obtain the maximum Reynolds number possible, measurements were taken at 50 m s<sup>-1</sup>, nearly the highest free-stream velocity of the tunnel. At this speed we have a fairly well-defined inertial sub-range, but owing to the above hot-wire anemometry limitation it is not possible to resolve the dissipation range. Our feasibility studies had also shown that at this high free-stream velocity spatial resolution in the dissipation range was a problem. Second, to allow accurate measurement of the dissipation range, measurements were taken at a lower free-stream velocity, 10 m s<sup>-1</sup>, where the expected Kolmogorov frequency was of the order of 5 kHz. The  $f^2$  noise was thus avoided and very good spatial resolution was obtained without a large sacrifice in microscale Reynolds number, but with a shorter inertial range than that obtained at 50 m s<sup>-1</sup>. Hereinafter the data sets corresponding to free-stream velocities  $U_e \approx 50$  m s<sup>-1</sup> and 10 m s<sup>-1</sup> will be referred to as the high-speed and low-speed cases, respectively.

## 2.2. Instrumentation and procedure

The hot-wire instrumentation consisted of Dantec models 55P01 single-wire and 55P51 crossed-wire probes, modified to support 2.5 µm Platinum-plated Tungsten wires with an etched length of approximately 0.5 mm, TSI IFA-100 model 150 hot-wire bridges, and model 157 signal conditioners. The crossed-wire probes (in *UV*- and *UW*-modes)



were oriented nominally at  $\pm 45^\circ$  to the mean-flow direction and the separation of the sensors of each probe was also approximately 0.5 mm. The square-wave response of the anemometers was adjusted for optimum damping. Their frequency response was about 90 kHz at  $10 \text{ m s}^{-1}$  and better than 100 kHz at  $50 \text{ m s}^{-1}$ .

One single and two X-wires were calibrated before every measurement. The effective wire angles were determined through a  $\pm 20^\circ$  yaw calibration (Bradshaw 1971). The accuracy of the calibrations of the hot wires was checked at several velocities in the calibration tunnel before the start of the measurements. The calibrations were repeated whenever the velocities obtained by the hot wires differed from the actual velocities (obtained from dynamic-pressure measurements) by more than  $\pm 2.5\%$ . During the boundary-layer measurements the output mean voltages from the hot-wire anemometers were monitored to detect drift. The hot-wire errors (e.g. due to misalignment, etc.) can be identified by the spurious flow pitch and yaw angles measured by the X-wires in *UV*- and *UW*-mode respectively. These were generally less than  $2^\circ$ .

The hot-wire output voltages were digitized on a microcomputer equipped with two Adtek AD830 12-bit, sample-and-hold, analog-to-digital converters. Each converter supported 8 channels at a sampling rate of 330 kHz per channel (one of the fastest available). The high-pass and low-pass filters used were Frequency Devices model 9016 (Butterworth, 48dB/octave). To obtain the maximum possible signal-to-noise ratio, the mean voltages were sampled and removed from the signals (by means of the signal conditioners and the high-pass filters) and the remaining fluctuations were amplified by a factor of 100 to 200 before they were sampled. All of the analog signals were high-pass filtered at 0.1 Hz. During the measurements of the Reynolds-stress profiles – but not the spectra – signals were low-pass filtered at 10 kHz and 70 kHz for the free-stream velocities of  $10 \text{ m s}^{-1}$  and  $50 \text{ m s}^{-1}$  respectively.

To improve the bandwidth of the spectra at low frequencies, the data were obtained in three spectral bands. For the low-speed spectral measurements around the mid-layer, these three bands were 0.1 Hz–100 Hz, 0.1 Hz–1 kHz, and 0.1 Hz–10 kHz; these bands were chosen to resolve the large scales, inertial range and dissipation range respectively. As the wall is approached, the Kolmogorov frequency increases and for the measurements in this region the low-pass cut-off frequency was increased. The corresponding frequency bands for the high-speed case were 0.1 Hz–1 kHz, 0.1 Hz–20 kHz, and 0.1 Hz–100 kHz.

For the Reynolds-stress profiles, 50 records of 1024 samples each were taken at a sampling frequency of 500 Hz at each point across the layer. In general, for spectral measurements, 150 or 200 records of 4096 samples each were recorded in the low-frequency band and 300 or 400 such records in the higher-frequency bands. In every case, the sampling frequency was three to four times larger than the low-pass cut-off frequency in order to avoid aliasing errors.

The spectral density of each band was computed by a fast-Fourier-transform algorithm, and the portion of the spectrum that corresponded to frequencies higher than half the low-pass filter-cutoff frequency was deleted. Also, the lowest frequency accepted was 0.2 Hz, since the high-pass filter cut-off frequency was always set at 0.1 Hz. Thus discarding the highest and lowest octaves of the measured spectra ensured that none of the spectra was affected by the filter roll-off characteristics. Finally, for each point in the boundary layer, the three spectral segments were combined into a single spectrum, which retained extensive regions of overlap. Using Taylor's hypothesis, the wavenumber,  $k_1$ , was taken equal to  $2\pi f/U_c$ , where  $U_c$ , the local convection velocity, was assumed to be equal to the local mean velocity at the measurement point.

For the low-speed experiment, the time series were measured at  $y = 25, 100, 300, 515$  and  $900$  mm from the wall and for the high-speed case at  $y = 100, 400$  and  $800$  mm. To ensure the repeatability of the data, most of these measurements were taken at least twice (at some  $y$  positions the data were measured three or four times). As an example, Saddoughi (1992) has shown that the day-to-day variation among the spectral data taken at the highest Reynolds number with different sets of X-wires having different calibrations, was less than 10%. This was considered to be fairly good repeatability. Note that no correction was applied to the spectral data.

### 3. Results and discussion

The present experimental results are divided into 'large-scale' and 'small-scale' data. To determine the large-scale characteristics and obtain the parameters governing the development of the boundary layer, mean-flow velocity and Reynolds-stress profiles are analysed. Some of these data are compared with the results from other boundary-layer studies. These large-scale results facilitated the choice of points at which the small-scale measurements were taken.

Among the small scales we first study the dissipation range of the spectra. This is followed by an examination of Kolmogorov's inertial-subrange scaling laws for spectra and structure functions. Finally, a few consistency tests are applied to investigate the local-isotropy hypothesis more directly.

#### 3.1. Analysis of large-scale data

The normalized profiles of the longitudinal mean velocity,  $U/U_e$ , for both the high-speed and low-speed cases are plotted in figure 2 versus distance  $y$  from the wall. The accuracy of these data is  $\pm 3\%$ . Also shown in this figure is the least-square polynomial fit to the data (solid line), which has been used to obtain the mean-flow integral parameters for both cases. The excellent collapse of the two profiles with  $y$  indicates that the boundary-layer thickness  $\delta$  (the point where  $U/U_e = 0.995$ ) in both cases is the same ( $\delta \approx 1090$  mm) at this measurement location. For smooth-wall boundary layers at a fixed  $x$ , one would expect a 30% to 40% decrease in  $\delta$  for a five-fold increase in free-stream velocity. However, it appears that at this streamwise location the layers have grown over a rough surface of very great length (more than 60 m of rough-wall contraction followed by approximately 50 m of test section), and that the boundary-layer integral parameters have become independent of free-stream velocity. The displacement thickness,  $\delta^*$ , and momentum thickness,  $\theta$ , are approximately 156 mm and 111 mm respectively. The maximum Reynolds number based on momentum thickness is  $R_\theta \approx 370000$ , the highest ever attained in a laboratory boundary-layer flow.

One of the problems in rough-wall boundary-layer experiments is the accurate measurement of the local skin-friction coefficient,  $C_f$ , because in addition to  $C_f$  there are two other unknown variables that must be determined. These are the roughness function and the error in origin,  $e$  (Perry & Joubert 1963). The latter variable is the distance below the crests of the roughness elements that defines an origin that will give the profiles a logarithmic distribution of velocity near the wall. Perry & Li (1990) have developed a modified Clauser plot to find  $e$  that is based on the original method of Perry & Joubert. This method was used to estimate the values of the wall-friction velocities,  $U_\tau$ , for the present experiments. It is important to note that, for the current investigations, the  $U_\tau$  values are only used to estimate the values of  $y^+$  and as a scaling parameter when our large-scale mean results are compared to those for other boundary

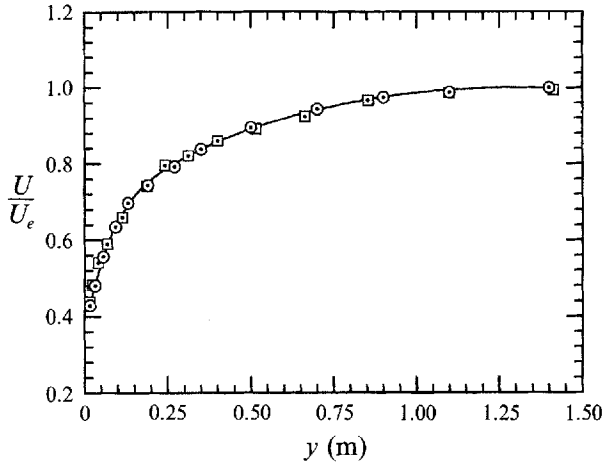


FIGURE 2. Normalized longitudinal mean-velocity profiles measured at two different free-stream velocities.  $\odot$ ,  $U_e \approx 50 \text{ m s}^{-1}$  ( $Re_\theta \approx 370\,000$ );  $\square$ ,  $U_e \approx 10 \text{ m s}^{-1}$  ( $Re_\theta \approx 74\,000$ ). The solid line is the least-square polynomial fit to the data.

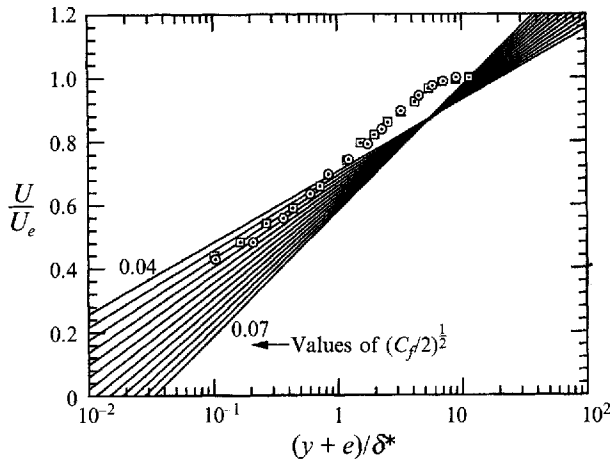


FIGURE 3. Mean-velocity profiles measured for two different free-stream velocities. ‘Modified Clauser chart’ method for rough-wall boundary layers (Perry & Li 1990).  $\delta^*$  is the displacement thickness, and each of the straight lines corresponds to a constant value of  $(C_f/2)^{1/2}$ . Error in origin,  $e = 1 \text{ mm}$ . For key to symbols see figure 2.

layers. As far as the scaling of the small-scale data is concerned, the friction velocity will not play any role – the only relevant mean-flow parameter is  $S = \partial U/\partial y$ , which is obtained by differentiating the least-square polynomial fit presented in figure 2.

Figure 3 shows the modified Clauser chart for rough-wall boundary layers and the present mean-velocity profiles with an error in origin,  $e = 1 \text{ mm}$ . Each of the straight lines corresponds to a constant value of  $(\frac{1}{2}C_f)^{1/2}$ . The profile shapes appear to be typical and, as expected from the collapse noted in figure 2, both have the same skin-friction coefficient; we estimate  $(U_\tau/U_e) = (\frac{1}{2}C_f)^{1/2} = 0.0465 \pm 2.5\%$ , since in that part of the plot the difference between two straight lines is about 5%.

The normalized profiles of the Reynolds normal stresses  $(\overline{u_1^2}/U_e^2, \overline{u_2^2}/U_e^2, \overline{u_3^2}/U_e^2)$  and the shear stress,  $-\overline{u_1 u_2}/U_e^2$ , are presented in figure 4 for both the high-speed and low-speed cases. These profiles also appear to be independent of free-stream velocity. In the

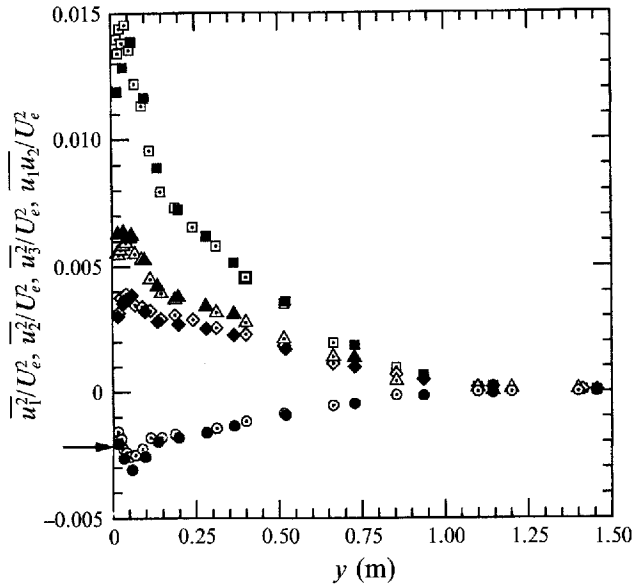


FIGURE 4. Profiles of Reynolds stresses measured for two different free-stream velocities. Solid and open symbols are for  $U_e \approx 50 \text{ m s}^{-1}$  ( $R_\theta \approx 370\,000$ ) and  $U_e \approx 10 \text{ m s}^{-1}$  ( $R_\theta \approx 74\,000$ ) respectively.  $\square$ ,  $u_1^2/U_e^2$ ;  $\diamond$ ,  $u_2^2/U_e^2$ ;  $\triangle$ ,  $u_3^2/U_e^2$ ;  $\circ$ ,  $u_1 u_2/U_e^2$ . The arrow shows the wall value obtained from the Clauser chart (figure 3).

outer part of the boundary layer, they have the standard shapes, but near the wall there appears to be a sharp rise in the values of all the stresses. We will not attempt to explain this anomalous behaviour, which presumably resulted from the acoustic panels. However, note that the Clauser-plot value of  $\frac{1}{2}C_f$  (shown in figure 4 by an arrow) agrees reasonably well with the shear-stress data.

To verify that the outer part of the present boundary layer did follow the standard turbulent boundary-layer behaviour, the Reynolds-shear-stress profiles, which are known to have the largest measurement uncertainty and are the most difficult to match among different experiments, are compared in figure 5 with the rough-wall profiles of Perry & Li (1990) and the smooth-wall profile of Morrison, Subramanian & Bradshaw (1992). In this figure,  $\delta_H$  is the Hama boundary-layer thickness,  $(U_e \delta^*)/(CU_\tau)$ , where  $C = 3.3715$ . For the present study  $\delta_H \approx 995 \text{ mm}$ . The data of figure 5(a) are replotted in figure 5(b) with a logarithmic axis to show the differences between the data sets close to the wall. There appears to be fairly good agreement between the present data and the other experiments in the outer part of the layer.

Dimensionless properties of the boundary layer, such as Townsend's structure parameter,

$$a_1 \equiv -\overline{u_1 u_2}/q^2, \quad (17)$$

are good indicators of the state of the large-scale structure of turbulence. The  $a_1$  values are shown in figure 6. In the canonical smooth-wall flat-plate boundary layer,  $a_1 \approx 0.13$  (Townsend 1976, p. 108), except near the surface and the outer edge. In the current investigations values close to the canonical ones are obtained.

### 3.2. Analysis of small-scale data

The small-scale measurements of the three components of velocity made for the low-speed case at  $y = 100$  and  $515 \text{ mm}$ , and for the high-speed case at  $y = 100$  and  $400 \text{ mm}$  are analysed here. These positions are away from the wall, so that the 'bump' in the

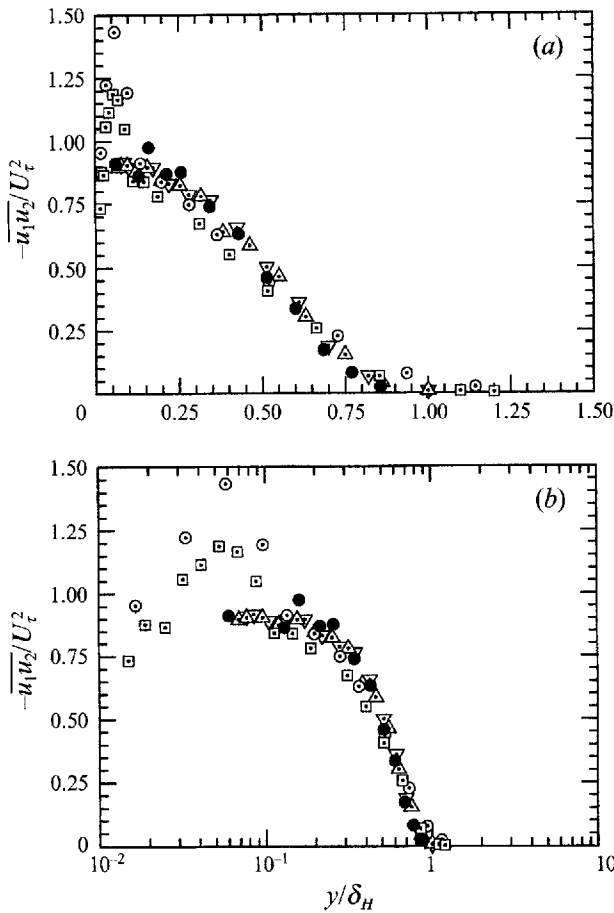


FIGURE 5. Comparison of the measured Reynolds shear stress,  $-\overline{u_1 u_2} / U_\tau^2$ :  $\odot$ , for  $R_\theta \approx 370000$  and  $\square$ , for  $R_\theta \approx 74000$ , with the rough-wall data of Perry & Li (1990):  $\nabla$ , for  $R_\theta = 2243$  and  $\triangle$ , for  $R_\theta = 2497$ , and the smooth-wall data of Morrison *et al.* (1992):  $\bullet$  for  $R_\theta = 14500$ . (a) Linear plot; (b) semi-log plot.

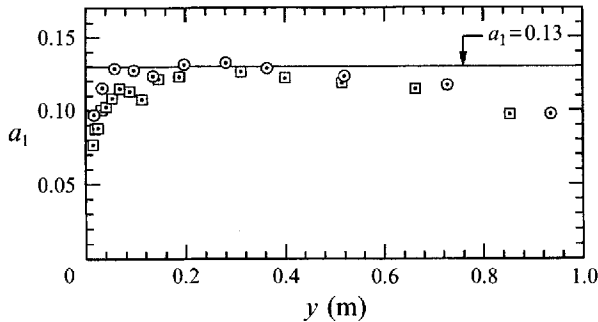


FIGURE 6. The structure parameter,  $a_1 \equiv -\overline{u_1 u_2} / q^2$ . The solid line is the canonical smooth-wall value (Townsend 1976). For key to symbols see figure 2.

Reynolds stresses is avoided. Hereinafter,  $y = 400$  and  $515$  mm will be referred to as mid-layer measurement positions and  $y = 100$  mm will be called the inner-layer position (since  $y / \delta < 0.2$ , and  $y^+ \approx 3000$  and  $\approx 16000$  for the low-speed and high-speed cases respectively). The relevant flow parameters at these  $y$  positions, including

Case	Low speed		High speed	
$U_e$ (m s <sup>-1</sup> )	10		50	
$\delta$ (mm)	1090		1090	
$\delta^*$ (mm)	156		156	
$\theta$ (mm)	111		111	
$(C_f/2)^{1/2}$	0.0465		0.0465	
$U_r$ (m s <sup>-1</sup> )	0.465		2.325	
$\delta_H$ (mm)	995		995	
$R_g$	74000		370000	
$y$ (mm)	100	515	100	400
$y^+$	3200	16200	16000	62000
$U$ (m s <sup>-1</sup> )	6.1	8.95	34.8	43.2
$S$ (s <sup>-1</sup> )	16.72	2.95	83.5	18.8
$\overline{u_1^2}$ (m <sup>2</sup> s <sup>-2</sup> )	0.87	0.343	26.0	9.5
$\overline{u_2^2}$ (m <sup>2</sup> s <sup>-2</sup> )	0.31	0.174	7.5	4.5
$\overline{u_3^2}$ (m <sup>2</sup> s <sup>-2</sup> )	0.48	0.212	13.0	5.95
$-\overline{u_1 u_2}$ (m <sup>2</sup> s <sup>-2</sup> )	0.213	0.085	4.64	2.31
$\overline{u_1^2}/U$	0.153	0.065	0.147	0.071
$q^2$ (m <sup>2</sup> s <sup>-2</sup> )	1.66	0.73	46.5	19.95
$\epsilon$ (m <sup>2</sup> s <sup>-3</sup> )	3.1	0.33	342	49
$\eta$ (mm)	0.18	0.32	0.055	0.09
Spatial resolution	2.8 $\eta$	1.5 $\eta$	9 $\eta$	5.5 $\eta$
$f_\eta$ (kHz)	5.5	4.5	100	76
$R_\lambda$	500	600	1400	1450
$S^*$	9.0	6.5	11.4	7.6
$S_c^*$	0.037	0.02	0.0175	0.0105
$(\epsilon/S^3)^{1/3}$ (m)	0.026	0.113	0.024	0.086

TABLE 1. Flow parameters

the large-scale parameters of the boundary layer at both free-stream velocities, are given in table 1. The accuracies of the parameter values are discussed in that section pertaining to each parameter. The data measured near the edge of the boundary layer, where external-intermittency effects are important, will be presented in another paper.

The mid-layer position is perhaps the best point at which to analyse the spectral results for the following reasons: (a) the r.m.s. longitudinal velocity fluctuation normalized by the local mean velocity,  $\overline{u_1^2}/U$ , is less than 0.1, so that errors arising from the use of Taylor's hypothesis are small (Lumley 1965; Wyngaard & Clifford 1977); (b) the Reynolds number

$$R_\lambda \equiv \overline{u_1^2} \lambda / \nu, \quad (18)$$

based on the Taylor microscale

$$\lambda \equiv [\overline{u_1^2} / (\overline{\partial u_1 / \partial x_1})^2]^{1/2} \quad (19)$$

appears to be close to its maximum value; (c) it is well inside the layer and boundary-layer edge intermittency effects are not present.

The position  $y = 100$  mm was also chosen for detailed measurements because we wanted to investigate the local-isotropy hypothesis in a region where the mean shear was larger than that at the mid-layer position. It is generally accepted (see e.g. Piomelli, Balint & Wallace 1989; Kim & Hussain 1993) that for wall-bounded flows Taylor's hypothesis is valid beyond the viscous region (say  $y^+ > 100$ ). However, for the present measurements at  $y = 100$  mm, where the local turbulence intensity is approximately

0.15, the errors arising from the use of Taylor's hypothesis can be calculated using the equations given by Wyngaard & Clifford (1977), which are based on an extension of Lumley's (1965) work. The necessary corrections are

$$E_{11}^{meas} = E_{11}^{true} \left( 1 - \frac{\overline{u_1^2}}{9U^2} + \frac{2\overline{u_2^2}}{3U^2} + \frac{2\overline{u_3^2}}{3U^2} \right), \quad (20)$$

and

$$E_{22}^{meas} = E_{22}^{true} \left( 1 - \frac{\overline{u_1^2}}{9U^2} + \frac{\overline{u_2^2}}{12U^2} + \frac{\overline{u_3^2}}{3U^2} \right), \quad (21)$$

for the longitudinal and transverse spectra in the inertial subrange respectively, and

$$\overline{[(\partial u_1/\partial x_1)^2]}^{meas} = \overline{[(\partial u_1/\partial x_1)^2]}^{true} \left( 1 + \frac{\overline{u_1^2}}{U^2} + \frac{2\overline{u_2^2}}{U^2} + \frac{2\overline{u_3^2}}{U^2} \right), \quad (22)$$

and

$$\overline{[(\partial u_2/\partial x_1)^2]}^{meas} = \overline{[(\partial u_2/\partial x_1)^2]}^{true} \left( 1 + \frac{\overline{u_1^2}}{U^2} + \frac{\overline{u_2^2}}{2U^2} + \frac{\overline{u_3^2}}{U^2} \right), \quad (23)$$

for the first-derivative variances. The errors in  $\overline{(\partial u_1/\partial x_1)^2}$  and  $\overline{(\partial u_2/\partial x_1)^2}$  for the present measurements at  $y = 100$  mm were less than 7% and 5% respectively. However, as will be shown later, at this  $y$  location most of the data in the dissipation range will be discarded owing to hot-wire spatial-resolution and anemometry problems. Therefore it is more important here to estimate the Taylor-hypothesis errors in the inertial subrange, where they were reduced to very small values: less than 2% and 1% for the longitudinal and the transverse spectra, respectively.

The  $u_i$ -spectra at the inner-layer positions are shown in figure 7 and at the mid-layer positions are shown in figure 8. These spectra are plotted versus frequency,  $f$ , to more easily identify the three spectral bands given in §2.2. Clearly, in each case the agreement between the three segments of the spectrum is very good.

The Kolmogorov frequency,  $f_\eta \equiv U/(2\pi\eta)$ , where  $\eta$  was calculated by using the isotropic relation (see next section for the estimation of dissipation) changed from approximately 100 kHz in the high-speed measurements to 4.5 kHz in the low-speed measurements (table 1). Because of the  $f^2$  behaviour of the tail of the spectrum, and also owing to lack of sufficient spatial resolution, only frequencies up to about 30 kHz could be resolved for the high-speed case. As explained earlier (§2.1), the dissipation range cannot be resolved for the high-speed case. However, it is important to bear in mind that the high-speed results are more appropriate for the investigation of inertial-subrange scaling because they are at a much higher  $R_\lambda$ . It will become clear in the following sections that without the measurements at  $50 \text{ m s}^{-1}$  in the inertial range, one might reach erroneous conclusions. The approximate values of  $R_\lambda$  estimated for the inner-layer and mid-layer positions of the high-speed case appear to be very close to each other. This is because the inner-layer position is in the vicinity of the 'bump' in the Reynolds stresses (see figure 5) where they start to deviate from the standard behaviour.

For the low-speed measurements five decades of frequency were obtained with no contamination from electronics noise. At the inner-layer position, owing to the lack of spatial resolution, we can trust our measurements only up to  $k_1 \eta \approx 0.7$ , but at the mid-layer position our best spatial resolution ( $1.5\eta$ ) is achieved. The dissipation spectra for this position are discussed in the next section.

Figure 9 shows Kolmogorov's universal scaling of the mid-layer one-dimensional

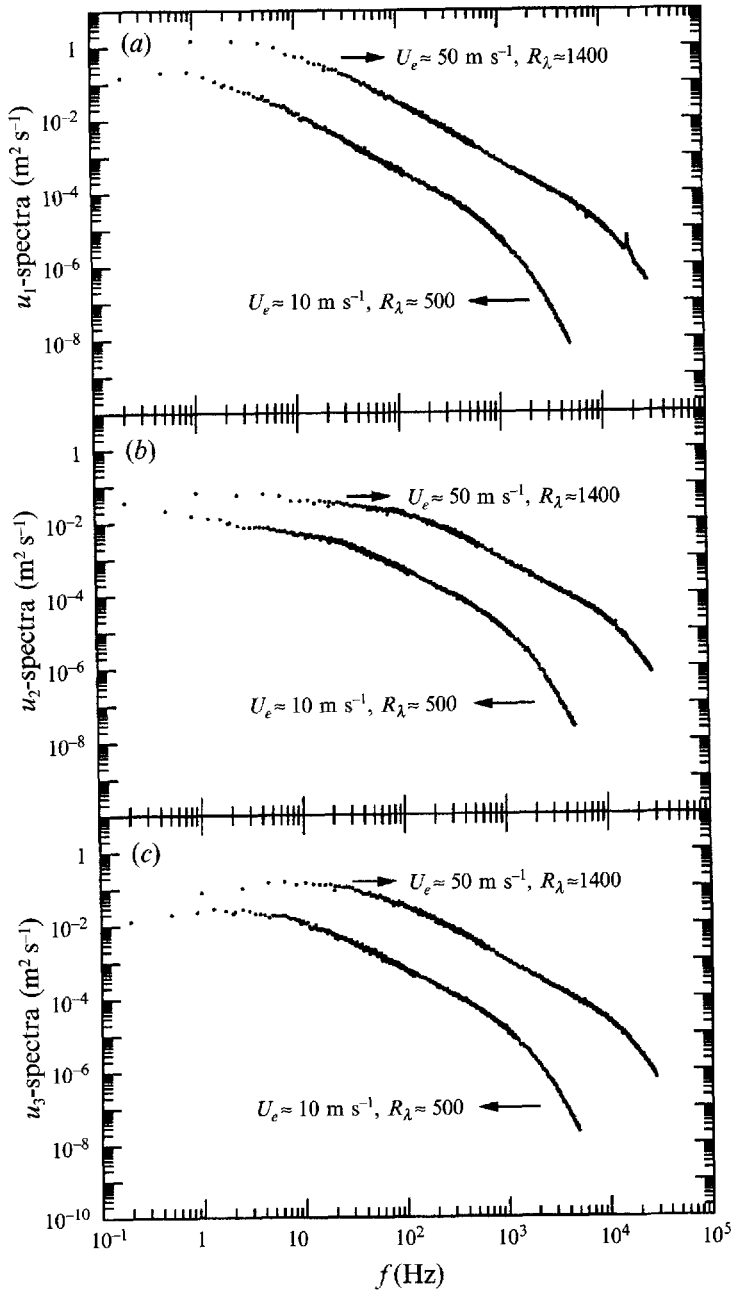


FIGURE 7. Longitudinal and transverse power spectra measured in the inner layer,  $y = 100$  mm, for two different free-stream velocities. For the low-speed case the measured frequency bands are 0.1 Hz–200 Hz, 0.1 Hz–2 kHz and 0.1 Hz–20 kHz, and the corresponding bands for the high-speed case are 0.1 Hz–1 kHz, 0.1 Hz–20 kHz and 0.1 Hz–100 kHz. (a)  $u_1$ -spectra; (b)  $u_2$ -spectra; (c)  $u_3$ -spectra.



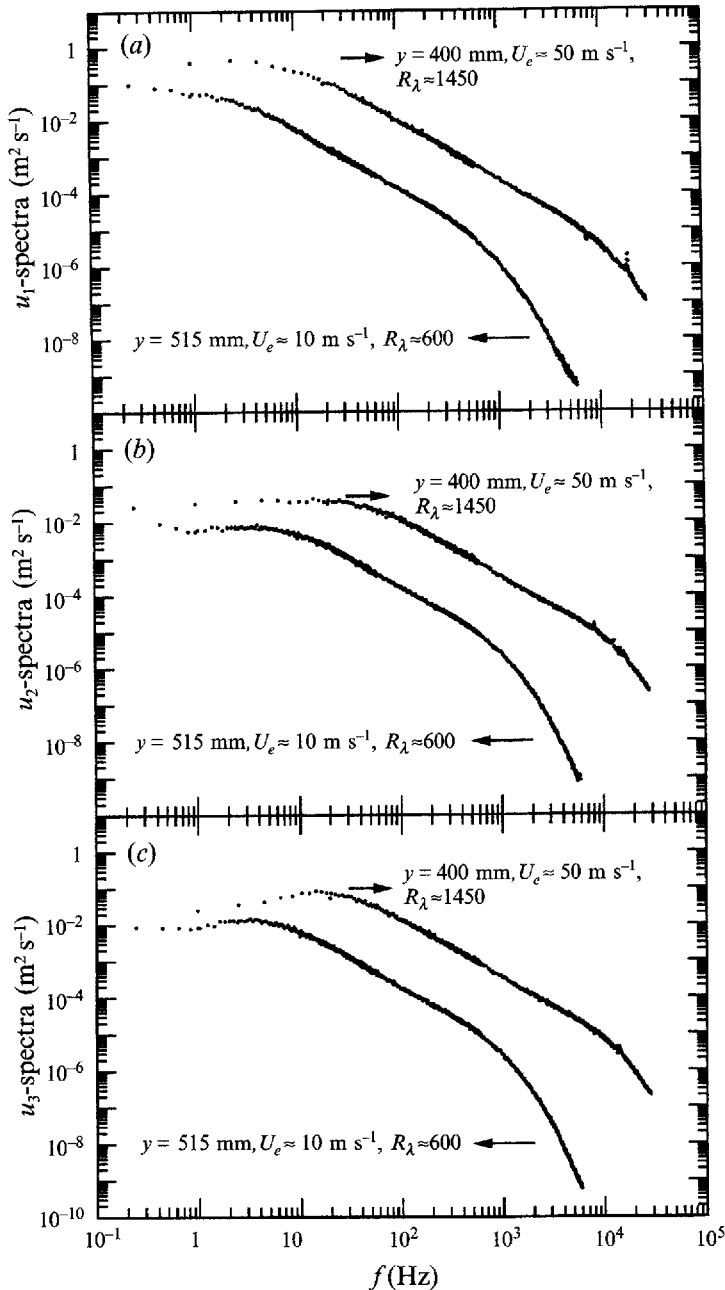


FIGURE 8. As figure 7 but at mid-layer,  $y = 400$  and  $515$  mm. For the low-speed case the measured frequency bands are  $0.1$  Hz– $100$  Hz,  $0.1$  Hz– $1$  kHz and  $0.1$  Hz– $10$  kHz, and the corresponding bands for the high-speed case are  $0.1$  Hz– $1$  kHz,  $0.1$  Hz– $20$  kHz and  $0.1$  Hz– $100$  kHz.

longitudinal power spectra compared to a compilation of previous experimental work taken from Chapman (1979) with later additions. Note that the extent of the  $-\frac{5}{3}$  range increases with Reynolds number. The present measurements encompass one of the largest scale ranges ever attained in laboratory flows.

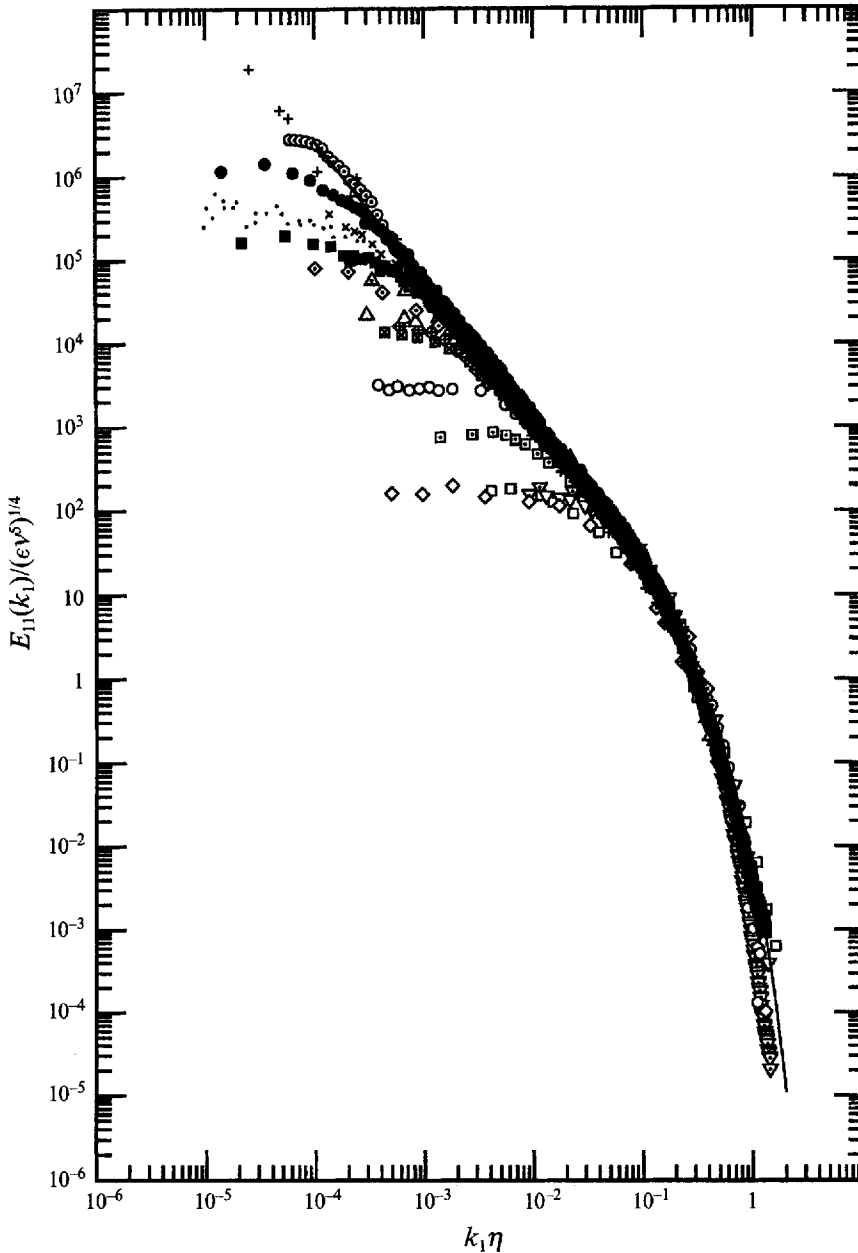


FIGURE 9. Kolmogorov's universal scaling for one-dimensional longitudinal power spectra. The present mid-layer spectra for both free-stream velocities are compared with data from other experiments. This compilation is from Chapman (1979), with later additions. The solid line is from Pao (1965).  $R_s$ :  $\square$ , 23 boundary layer (Tielman 1967);  $\diamond$ , 23 wake behind cylinder (Uberoi & Freymuth 1969);  $\nabla$ , 37 grid turbulence (Comte-Bellot & Corrsin 1971);  $\nabla$ , 53 channel centreline (Kim & Antonia (DNS) 1991);  $\square$ , 72 grid turbulence (Comte-Bellot & Corrsin 1971);  $\circ$ , 130 homogeneous shear flow (Champagne *et al.* 1970);  $\boxtimes$ , 170 pipe flow (Laufer 1954);  $\diamond$ , 282 boundary layer (Tielman 1967);  $\diamond$ , 308 wake behind cylinder (Uberoi & Freymuth 1969);  $\triangle$ , 401 boundary layer (Sanborn & Marshall 1965);  $\triangle$ , 540 grid turbulence (Kistler & Vrebalovich 1966);  $\times$ , 780 round jet (Gibson 1963);  $\cdot$ , 850 boundary layer (Coantic & Favre 1974);  $+$ ,  $\sim 2000$  tidal channel (Grant *et al.* 1962);  $\circ$ , 3180 return channel (CAHI Moscow 1991);  $\bullet$ , 1500 boundary layer (present data, mid-layer:  $U_e = 50 \text{ m s}^{-1}$ );  $\blacksquare$ , 600 boundary layer (present data, mid-layer:  $U_e = 10 \text{ m s}^{-1}$ ).

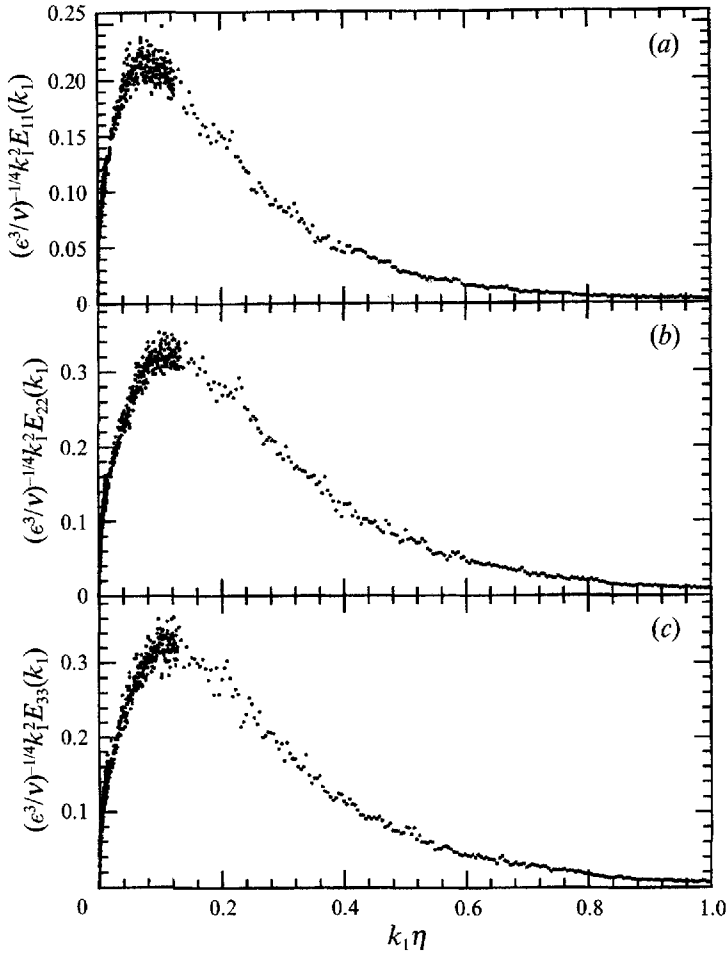


FIGURE 10. Dissipation spectra measured at mid-layer for the low-speed case ( $y = 515$  mm,  $R_\lambda \approx 600$ ). (a)  $u_1$ -spectrum; (b)  $u_2$ -spectrum; (c)  $u_3$ -spectrum.

### 3.2.1. Dissipation range

At the mid-layer position of the low-speed case ( $y = 515$  mm,  $R_\lambda \approx 600$ ), dissipation spectra given by the isotropic relation (Batchelor 1953)

$$\epsilon = 15\nu \int_0^\infty k_1^2 E_{11}(k_1) dk_1 = \frac{15}{2}\nu \int_0^\infty k_1^2 E_{22}(k_1) dk_1 = \frac{15}{2}\nu \int_0^\infty k_1^2 E_{33}(k_1) dk_1, \quad (24)$$

are plotted in non-dimensional form in figure 10. From the areas (before normalization) under the curves (a), (b) and (c) the values of  $(\partial u_1/\partial x_1)^2$ ,  $(\partial u_2/\partial x_1)^2$ , and  $(\partial u_3/\partial x_1)^2$ , respectively, can be calculated. It is clear that for this case the entire significant range of the dissipation spectrum is obtained. The scatter of the data around the peak is the result of superimposing the three measurement segments. This scatter is about  $\pm 10\%$  and, as will be shown later, the data for  $k_1\eta > 0.8$  may not be reliable. The integration over the third-spectral band of this data, which covered the entire frequency range of interest, satisfied (24) to within  $10\%$ ; the dissipation value obtained from the single-wire data shown in figure 10(a) is  $\epsilon \approx 0.33 \text{ m}^2 \text{ s}^{-3}$ . Similar integrations were performed for the inner-layer position of the low-speed case and satisfied (24) to within  $15\%$ . There the dissipation value is  $\epsilon \approx 3.1 \text{ m}^2 \text{ s}^{-3}$ .

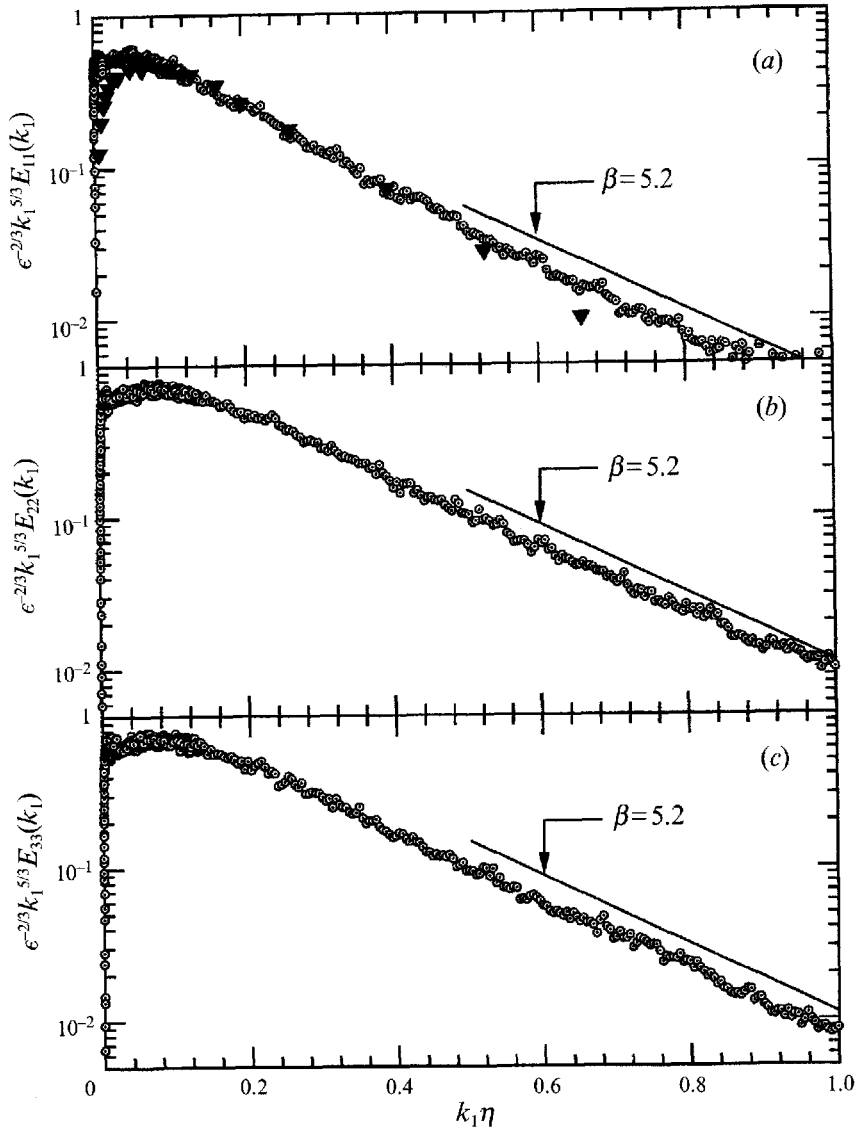


FIGURE 11. Compensated spectra in the dissipation range. (a)  $u_1$ -spectra; (b)  $u_2$ -spectrum; (c)  $u_3$ -spectrum.  $\odot$ , Mid-layer position for the low-speed case ( $y = 515$  mm,  $R_\lambda \approx 600$ );  $\blacktriangledown$ , Comte-Bellot & Corrsin (1971) for isotropic grid turbulence at  $R_\lambda = 60.7$ .

Kraichnan (1959) proposed that the dissipation range of the three-dimensional energy spectrum has a simple exponential decay with an algebraic prefactor of the form

$$E(k) = A(k\eta)^\gamma \exp[-\beta(k\eta)]. \quad (25)$$

Since then this form has also been found in direct numerical simulations, but necessarily at low Reynolds numbers, by other researchers, who have proposed that for  $0.5 \leq k\eta \leq 3$ ,  $\beta \approx 5.2$  (Kida & Murakami 1987; Kerr 1990; Sanada 1992; Kida *et al.* 1992). Recently Chen *et al.* (1993) have studied the far dissipation range of isotropic turbulence at a very low Reynolds number ( $R_\lambda = 15$ ) by direct numerical simulation. They confirmed the above exponential decay, but obtained  $\beta \approx 7.1$  for  $5 \leq k\eta \leq 10$ . It can be readily seen that for locally isotropic turbulence, the form of (25) and the

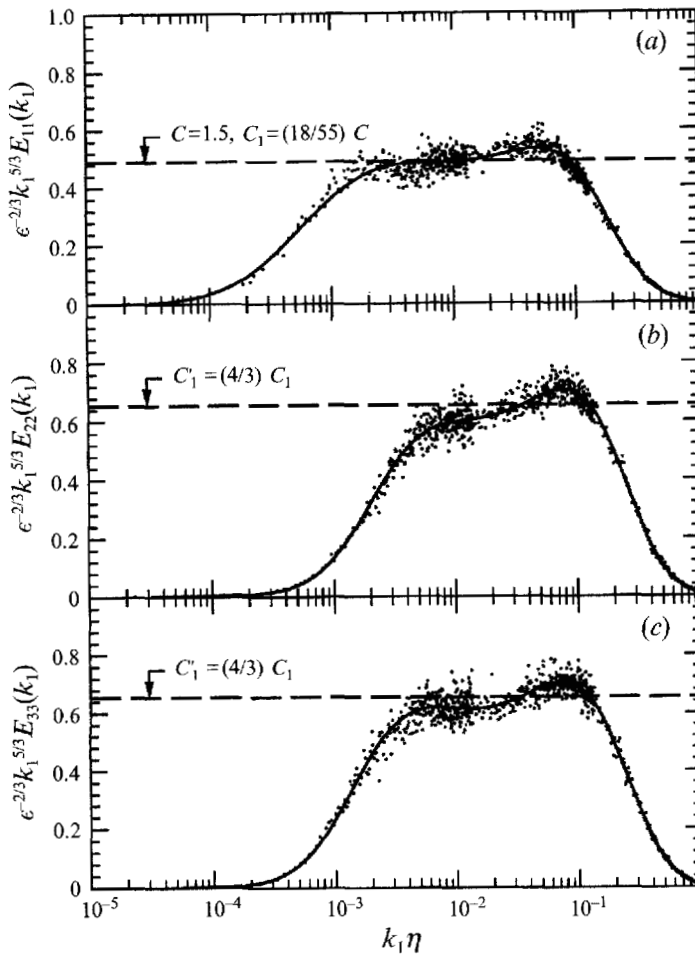


FIGURE 12. Compensated longitudinal and transverse spectra measured at mid-layer for the low-speed case ( $y = 515$  mm,  $y^+ \approx 16200$ ,  $R_\lambda \approx 600$ ). Only the data for wavenumber range  $k_1 \eta < 0.85$  can be accepted. Solid lines are the ninth-order, least-square, log-log polynomial fits to the spectral data. (a)  $u_1$ -spectrum; (b)  $u_2$ -spectrum; (c)  $u_3$ -spectrum.

numerical value of  $\beta$ , whatever it may be, should be preserved for all three one-dimensional spectra. The exponential form for the  $u_1$ -spectrum in the dissipation range was observed in experiments by Sreenivasan (1985), but he proposed  $\beta = 8.8$  for  $0.5 \leq k_1 \eta \leq 1.5$ .

To investigate the behaviour of the dissipation range, compensated spectra can be defined as  $e^{-\alpha k_1^2} E_{\alpha\alpha}(k_1)$ , where  $\alpha = 1, 2$  or  $3$  (no summation over  $\alpha$ ). Plots of these spectra at mid-layer for  $R_\lambda \approx 600$  are shown in figure 11. As can be seen in this figure, the  $u_1$ -spectrum (single wire) in the range  $k_1 \eta > 0.8$  is affected by noise and/or lack of resolution; however, this behaviour does not appear in the  $u_2$ - and  $u_3$ -spectra (crossed-wire). The present  $u_1$ -spectrum is compared to the data of Comte-Bellot & Corrsin (1971) for isotropic grid turbulence at  $R_\lambda = 60.7$ . In the dissipation range for  $k_1 \eta < 0.5$  the agreement between the two  $u_1$ -spectra appears to be good, but they deviate for  $k_1 \eta > 0.5$ . However, it appears that all three components of spectra for the current boundary-layer measurements show an essentially exponential decay and follow reasonably well the (DNS) straight lines with  $\beta = 5.2$  for  $0.5 \leq k_1 \eta \leq 1$ .

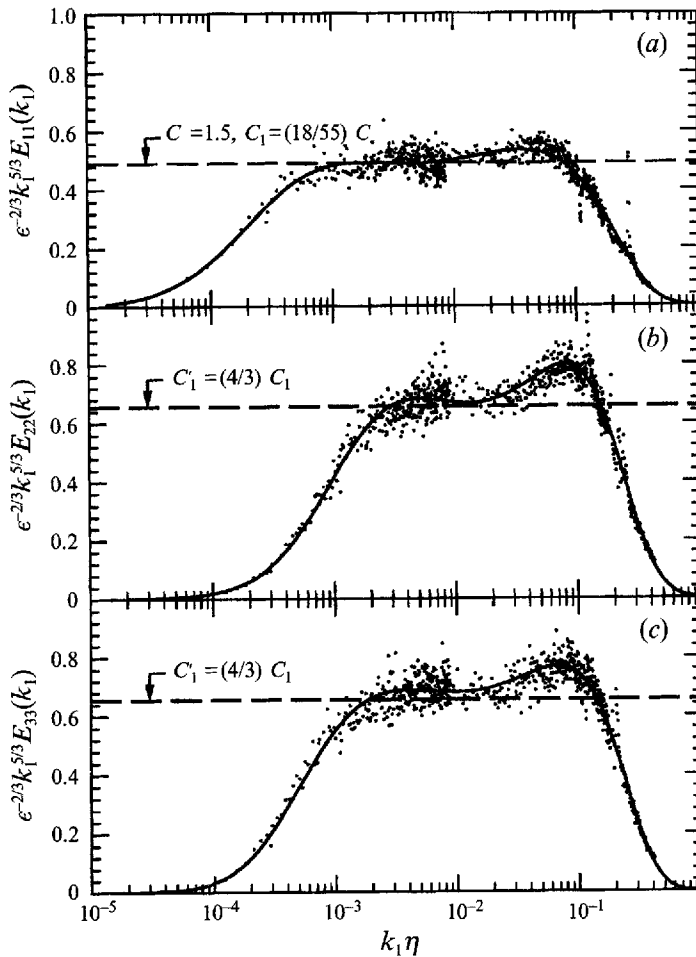


FIGURE 13. Compensated longitudinal and transverse spectra measured at mid-layer for the high-speed case ( $y = 400$  mm,  $y^+ \approx 62000$ ,  $R_\lambda \approx 1450$ ). Only the data for wavenumber range  $k_1 \eta < 0.25$  can be accepted. Solid lines are the ninth-order, least-square, log-log polynomial fits to the spectral data. (a)  $u_1$ -spectrum; (b)  $u_2$ -spectrum; (c)  $u_3$ -spectrum.

### 3.2.2. Inertial subrange

To investigate the validity of (7) and (8) in the inertial subrange, we again analyse the compensated spectra  $\epsilon^{-2/3} k_1^{5/3} E_{\alpha\alpha}(k_1)$ . In the inertial subrange, these should be independent of wavenumber and equal to the Kolmogorov's constants for one-dimensional spectra.

In figure 12 the compensated longitudinal and transverse spectra at the mid-layer position in the low-speed case, are plotted against  $k_1 \eta$ . The compensated ninth-order, least-square polynomial log-log fits of  $E_{\alpha\alpha}(k_1)$  presented in this figure prove to be very instructive in analysing the data. Here the dissipation value ( $\epsilon \approx 0.33$  m<sup>2</sup> s<sup>-3</sup>) obtained in the previous section is used.

For the  $u_1$ -spectrum there is slightly less than one decade of  $-\frac{5}{3}$  range, and in that wavenumber range the classical value for the Kolmogorov constant,  $C = 1.5$  (i.e.  $C_1 = 18C/55 = 0.491$ ) (Monin & Yaglom 1975) agrees very well with the present data. Noting that our dissipation accuracy was  $\pm 10\%$ , this gives  $C = 1.5 \pm 0.1$ . The  $u_3$ -spectrum exhibits more than half a decade of  $-\frac{5}{3}$  range, with an amplitude equal to  $\frac{4}{3}$

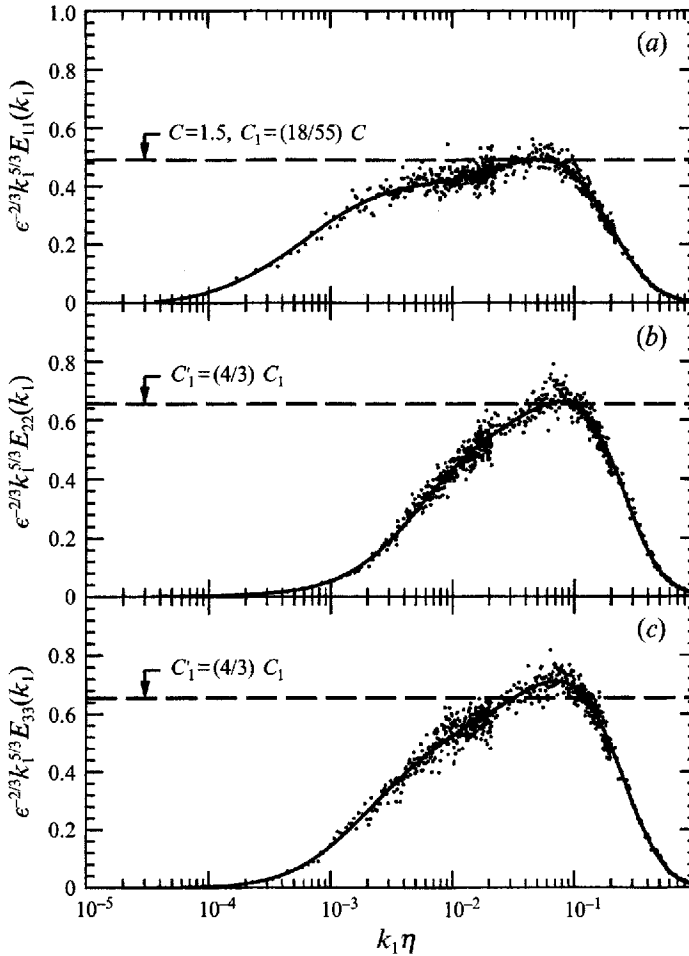


FIGURE 14. Compensated longitudinal and transverse spectra measured in the inner-layer for the low-speed case ( $y = 100$  mm,  $y^+ \approx 3200$ ,  $R_\lambda \approx 500$ ). Only the data for wavenumber range  $k_1 \eta < 0.45$  can be accepted. Solid lines are the ninth-order, least-square, log-log polynomial fits to the spectral data. (a)  $u_1$ -spectrum; (b)  $u_2$ -spectrum; (c)  $u_3$ -spectrum.

times that of the  $u_1$ -spectrum (the difference between the flat region of the  $u_3$ -spectrum and the isotropic line is within the accuracy range of the dissipation value). However, it appears that in this low-speed case, the  $u_2$ -spectrum does not show a perfectly flat region. It will be shown later that, at this  $y/\delta$  position, this is a Reynolds-number effect.

All three compensated spectra have a 'bump' between the inertial subrange and the dissipation range. These bumps have also been observed in other experiments (Williams & Paulson 1978 and Champagne *et al.* 1977 for temperature variance spectra; Mestayer 1982 for velocity spectra) and in theoretical predictions such as Eddy-Damped Quasi-Normal Markovian (EDQNM), as discussed by Mestayer, Chollet & Lesieur (1984). We believe that they are real.

For the high-speed data, a good direct estimate for dissipation is not possible. Therefore, we plotted  $k_1^{5/3} E_{11}(k_1)$  versus  $k_1$  (not shown here). From (7) we can see that in the inertial subrange the flat region should be equal to  $C_1 \epsilon^{2/3}$ . Since our low-speed data indicated that  $C = 1.5 \pm 0.1$ , we used this value and the above plot to calculate  $\epsilon \approx 49 \text{ m}^2 \text{ s}^{-3}$ . Using this value for the dissipation, the compensated spectra and their ninth-order polynomial fits at the mid-layer position in the high-speed case, are plotted

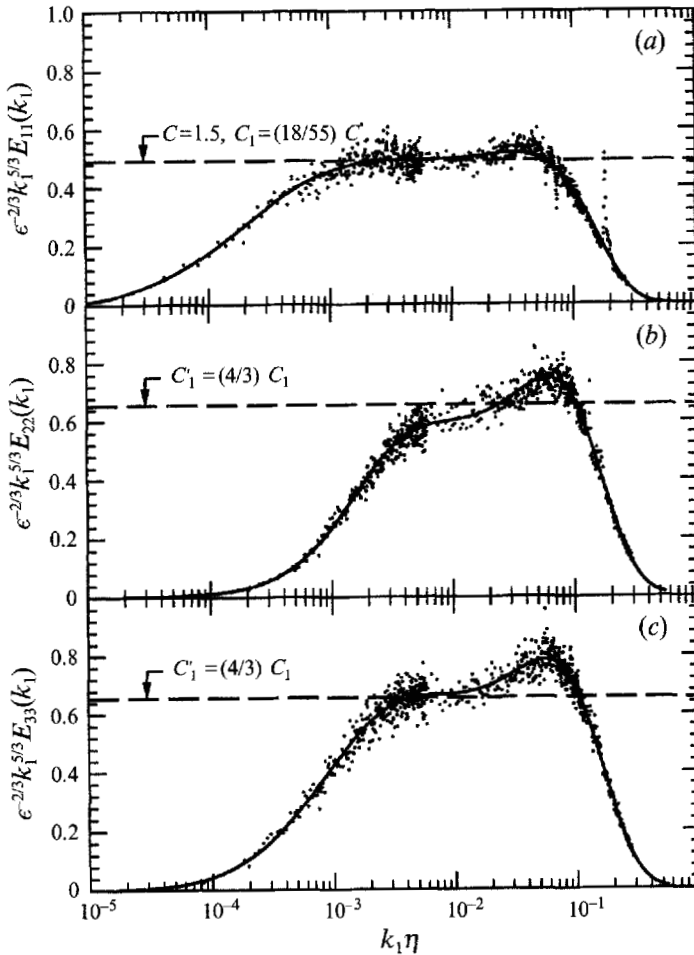


FIGURE 15. Compensated longitudinal and transverse spectra measured in the inner-layer for the high-speed case ( $y = 100$  mm,  $y^+ \approx 16000$ ,  $R_1 \approx 1400$ ). Only the data for wavenumber range  $k_1 \eta < 0.15$  can be accepted. Solid lines are the ninth-order, least-square, log-log polynomial fits to the spectral data. (a)  $u_1$ -spectrum; (b)  $u_2$ -spectrum; (c)  $u_3$ -spectrum.

in figure 13. It can be seen from this figure that at this higher  $R_\lambda$ , the compensated  $u_1$ -spectrum exhibits more than one decade of  $-\frac{5}{3}$  range, but less than the log-log plot (figure 9) suggested. Here, the  $u_2$ -spectrum, as well as the  $u_3$ -spectrum, contain well-defined  $-\frac{5}{3}$  ranges. They are, as expected, equal to each other and are larger than the  $u_1$ -spectrum by the  $\frac{4}{3}$  factor. The 'bumps' again appear on all three spectra, at almost the same  $k_1 \eta$  as in the low-speed case. There is no indication that the amplitude of the bump reduces with increasing Reynolds number once a well-defined inertial subrange is present.

The spectral data measured at the inner-layer position in the low-speed and high-speed cases are shown in figures 14 and 15 respectively. The dissipation value for the low-speed case was obtained in the previous section ( $\epsilon \approx 3.1 \text{ m}^2 \text{ s}^{-3}$ ), and the same method used to estimate the dissipation value at the mid-layer position in the high-speed case was employed here, which gave  $\epsilon \approx 342 \text{ m}^2 \text{ s}^{-3}$ . Differences between the low-speed and high-speed cases can be clearly seen at the inner-layer position. In figure 15, well-defined  $-\frac{5}{3}$  ranges for the  $u_1$ - and  $u_3$ -spectra are evident, whereas in figure 14 no such range can be seen.



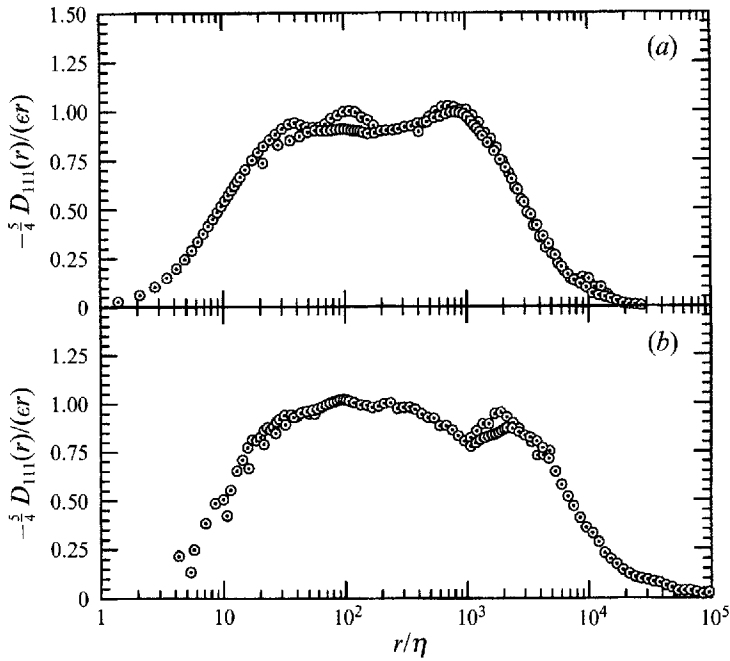


FIGURE 16. Compensated third-order structure functions for longitudinal velocity fluctuations measured at mid-layer. (a) Low-speed case ( $y = 515$  mm,  $y^+ \approx 16200$ ,  $R_\lambda \approx 600$ ); (b) high-speed case ( $y = 400$  mm,  $y^+ \approx 62000$ ,  $R_\lambda \approx 1450$ ).

The above figures illustrate several important points. They show rather clearly the order in which the different velocity component variances deviate from the  $-\frac{5}{3}$  law at low wavenumbers, either when the free-stream velocity is decreased or when the wall is approached ( $u_2$  deviates first, then  $u_3$ , and then  $u_1$ ). Comparison of the data taken at the same  $y/\delta$  position, but at a different free-stream velocity (figures 14 and 15) shows the effects of Reynolds number and  $S_c^*$  on the inertial ranges of the spectra. Perhaps a more important comparison is between figures 12 and 15, which are for two different  $y/\delta$  positions and Reynolds numbers (mid-layer of the low-speed run and the inner-layer of the high-speed run respectively), but for the same  $y^+ \approx 16000$  and  $S_c^* \approx 0.02$ . The apparent similarity between the inertial ranges of the spectra suggests that their behaviour depends only on  $S_c^*$ . These observations indicate that only linear-log plots of compensated spectra can clearly show the intricate behaviour in the inertial subrange, and any claim for the existence of an inertial subrange should be substantiated by that kind of plot.

The inertial subrange was also investigated for consistency with Kolmogorov's scaling laws for the structure functions, given by (12), (13) and (14). A plot of the third-order structure function for the longitudinal velocity fluctuations,  $-\frac{5}{4}r^{-1}D_{111}(r)$  versus  $r$ , should be equal to  $\epsilon$  and independent of  $r$  in the inertial subrange. This type of plot (not shown) was used to calculate  $\epsilon \approx 0.26$  m<sup>2</sup> s<sup>-3</sup> and  $\approx 40$  m<sup>2</sup> s<sup>-3</sup> for the low-speed and high-speed cases respectively, which are about 20% lower than those estimated from the spectra. The microscale Reynolds numbers obtained using these dissipations were approximately 670 and 1500 for the low-speed and high-speed cases respectively. Using these dissipation values, the compensated third-order structure functions at the mid-layer positions are presented in figure 16. The values of the separation  $r$  were calculated using Taylor's hypothesis,  $r = \tau U$ , where  $\tau$  is the time interval and  $U$  is the local mean velocity. Again it is important that the log-linear plots of these structure

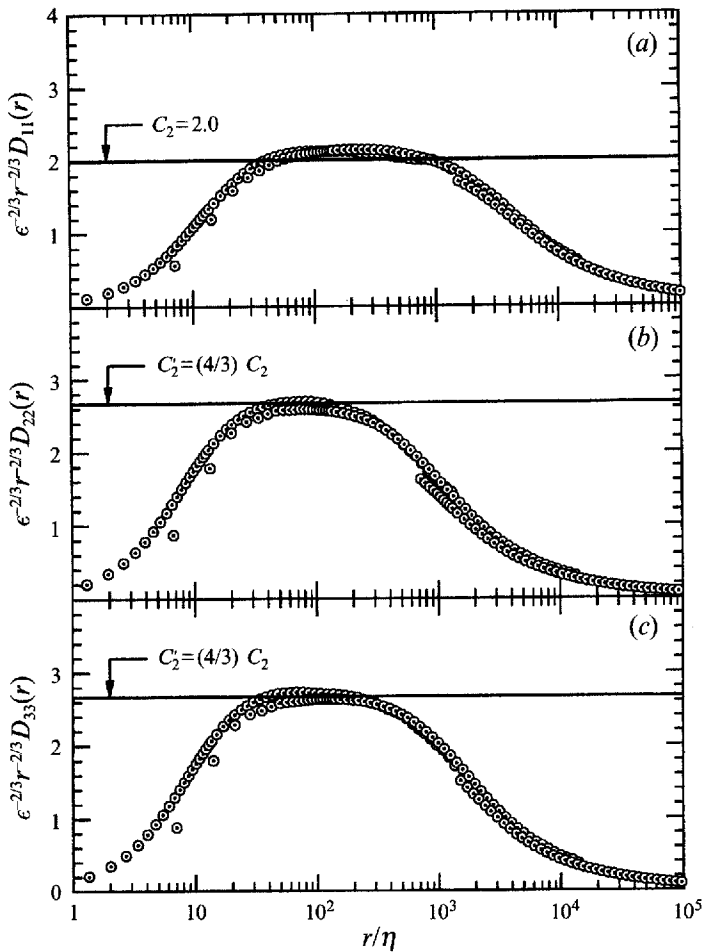


FIGURE 17. Compensated second-order structure functions for longitudinal and transverse velocity fluctuations measured at mid-layer for the low-speed case ( $y = 515$  mm,  $y^+ \approx 16200$ ,  $R_\lambda \approx 600$ ). Dissipation is from the third-order structure function. (a)  $u_1$ -structure function; (b)  $u_2$ -structure function; (c)  $u_3$ -structure function.

functions be investigated, rather than the customary log-log plots which tend to mask the variations that may exist in the inertial subrange. In this figure, as explained in §2.1, there are three different data sets corresponding to the three measurement bands used for resolving the large scales, the inertial subrange and the dissipation range. Note that these are the actual data and not polynomial fits. The low-speed case and the high-speed case show about one-and-a-half and two decades of relatively flat regions respectively.

Using the dissipation values obtained from the third-order structure functions, the compensated second-order structure functions are plotted in figures 17 and 18 for the low-speed and high-speed cases respectively. The three components of the second-order structure functions exhibit inertial subranges, although the  $u_2$ -component for the low-speed case shows the least extent. At a given Reynolds number, the  $u_2$ - and  $u_3$ -structure functions in the inertial subrange are equal to each other and are larger than the  $u_1$ -structure function by the factor  $\frac{4}{3}$ , to within the measurement accuracy. For the low-speed case the data agree very well with the Kolmogorov constant  $C_2 = 2.0$ , which corresponds to  $C = 1.5$ . For the high-speed case, the deviation of the horizontal lines

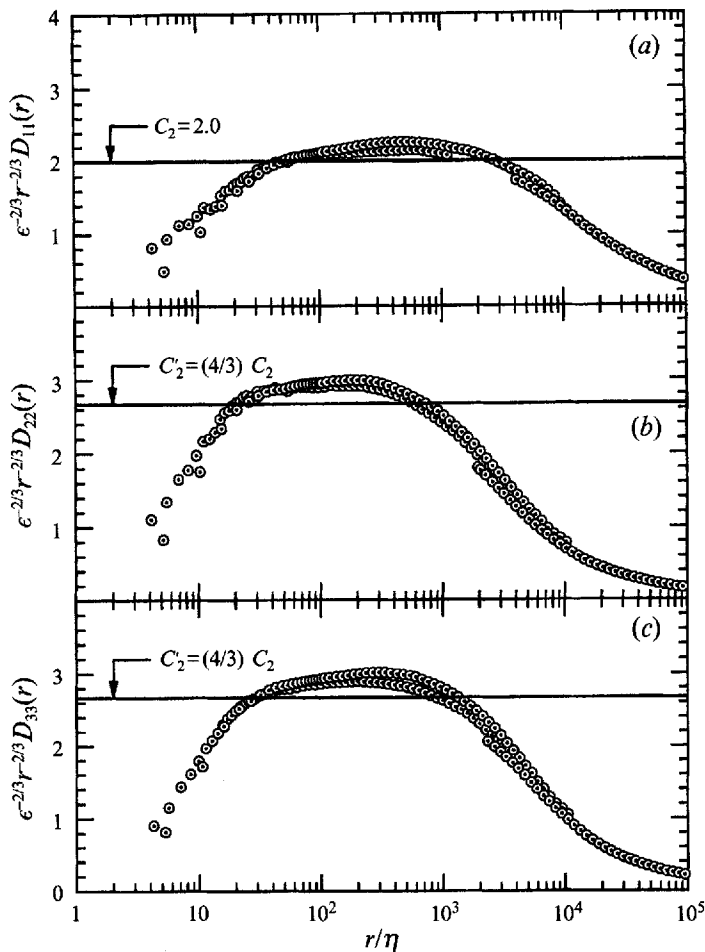


FIGURE 18. Compensated second-order structure functions for longitudinal and transverse velocity fluctuations measured at mid-layer for the high-speed case ( $y = 400$  mm,  $y^+ \approx 62000$ ,  $R_\lambda \approx 1450$ ). Dissipation is from the third-order structure function. (a)  $u_1$ -structure function; (b)  $u_2$ -structure function; (c)  $u_3$ -structure function.

from the plateau regions is equivalent to a 10% change in the dissipation. Therefore, we estimate  $C_2 = 2.0 \pm 0.1$ .

### 3.2.3. Tests of the local-isotropy hypothesis

The main aim of the present investigation has been to study the effects of mean-strain rate ( $S = \partial U / \partial y$ ) on the local isotropy. The parameters characterizing these effects were identified as  $S^* \equiv S q^2 / \epsilon$  and  $S_c^* \equiv S(\nu / \epsilon)^{1/2}$ . In general, there is some degree of uncertainty associated with the experimental estimations of  $S^*$  and  $S_c^*$  because they involve gradients calculated from data points that are widely spaced and, at best, the dissipation values for the present cases are accurate to 20%. However, it is clear that the uncertainty in  $S_c^*$  is less than that in  $S^*$ .

To calculate these parameters, we have used the dissipation values obtained from the spectral measurements and values of  $S$  obtained by differentiating the least-square polynomial fit to the mean-velocity profiles (figure 2). The values of these parameters are given in table 1. By virtue of the fact that our experiments were conducted at high

Reynolds numbers and all of the measurement points were beyond the sublayer (minimum  $y^+ > 3000$ ), the Corrsin-Uberoi condition  $S_c^* \ll 1$  is satisfied and we should expect local isotropy at high wavenumbers in the mixed range of spectra. However, the question is, once the above condition is satisfied, over what wavenumber range can one expect local isotropy in the inertial subrange? These issues are addressed here.

Onsager (1949) used dimensional arguments to define the characteristic inertial transfer time per stage as

$$\tau_\alpha(k) \equiv 1/[k^3 E(k)]^{\frac{1}{2}}. \quad (26)$$

Corrsin (1958) proposed that in thin shear flows where  $\frac{1}{2}S$  is a good approximation to the principal mean-strain rate, a necessary condition for the existence of local isotropy is that  $\tau_\alpha$  should be much smaller than the characteristic mean-strain time,  $(\frac{1}{2}S)^{-1}$ . Therefore, local isotropy can be expected when

$$1/[k^3 E(k)]^{\frac{1}{2}} \ll 1/(\frac{1}{2}S). \quad (27)$$

In an inertial subrange  $\tau_\alpha(k)$  then decreases monotonically as  $\epsilon^{-\frac{1}{3}}k^{-\frac{2}{3}}$ , and (27) becomes

$$k^{\frac{2}{3}} \gg \frac{1}{2}\epsilon^{-\frac{1}{3}}S, \quad (28)$$

which gives the condition for local isotropy within an inertial range in terms of wavenumber. The above relation can be rewritten in terms of non-dimensional wavenumber as

$$k(\epsilon/S^3)^{\frac{1}{2}} \gg \left(\frac{1}{2}\right)^{\frac{3}{2}}, \quad (29)$$

using the lengthscale  $(\epsilon/S^3)^{\frac{1}{2}}$ . The above arguments are applicable for one-dimensional spectra, but the numerical value in (29) will be different.

Based on dimensional analysis, Lumley (1967) argued that when  $k$  is much larger than  $(S^3/\epsilon)^{\frac{1}{2}}$ , but small compared to the Kolmogorov wavenumber, the shear-stress cospectrum should scale linearly with  $S$  as

$$-E_{12}(k) = C_0 \epsilon^{\frac{1}{3}} \kappa^{-\frac{2}{3}} S, \quad (30)$$

where  $C_0$  is a constant. Wyngaard & Cote (1972) expanded the above arguments and included the effects of buoyancy and potential temperature gradient in (30). For one-dimensional cospectra, the same power-law relation as (30) should apply. Measurements in atmospheric boundary layers (see e.g. Pond *et al.* 1971; Caughey, Wyngaard & Kaimal 1979) have shown agreement with the above power law.

Shear-stress cospectra measured at different location in the boundary layer for both free-stream velocities are shown in figure 19. Parts (a) and (b) of this figure show the raw data for mid-layer and inner-layer positions respectively, and part (c) shows the collapse achieved by using  $(\epsilon/S^3)^{\frac{1}{2}}$  and  $(\epsilon/S)^{\frac{1}{2}}$  as length and velocity scales respectively. At the low-wavenumber end for a given  $y/\delta$ , the data collapse independent of Reynolds number and  $y^+$ . The cospectra do apparently exhibit the  $-\frac{7}{3}$  law and scale with  $S$  in the inertial subrange. Part (c) also indicates that the  $-\frac{7}{3}$  range starts at a non-dimensional wavenumber  $k_1(\epsilon/S^3)^{\frac{1}{2}} \approx 1$ . The value of the constant for one-dimensional cospectra obtained by Wyngaard & Cote (1972) was approximately equal to 0.15, which agree very well with the present measurements.

Note that only data for the low-wavenumber range and parts of the inertial subrange are shown in figure 19 because at high wavenumbers, where local isotropy is approached, the values of these cospectra become very small and experimental values occur with both signs. These are best discussed in terms of the correlation-coefficient spectra  $R_{12}(k_1)$  given by (10). If spectra contain well-defined inertial subranges, such

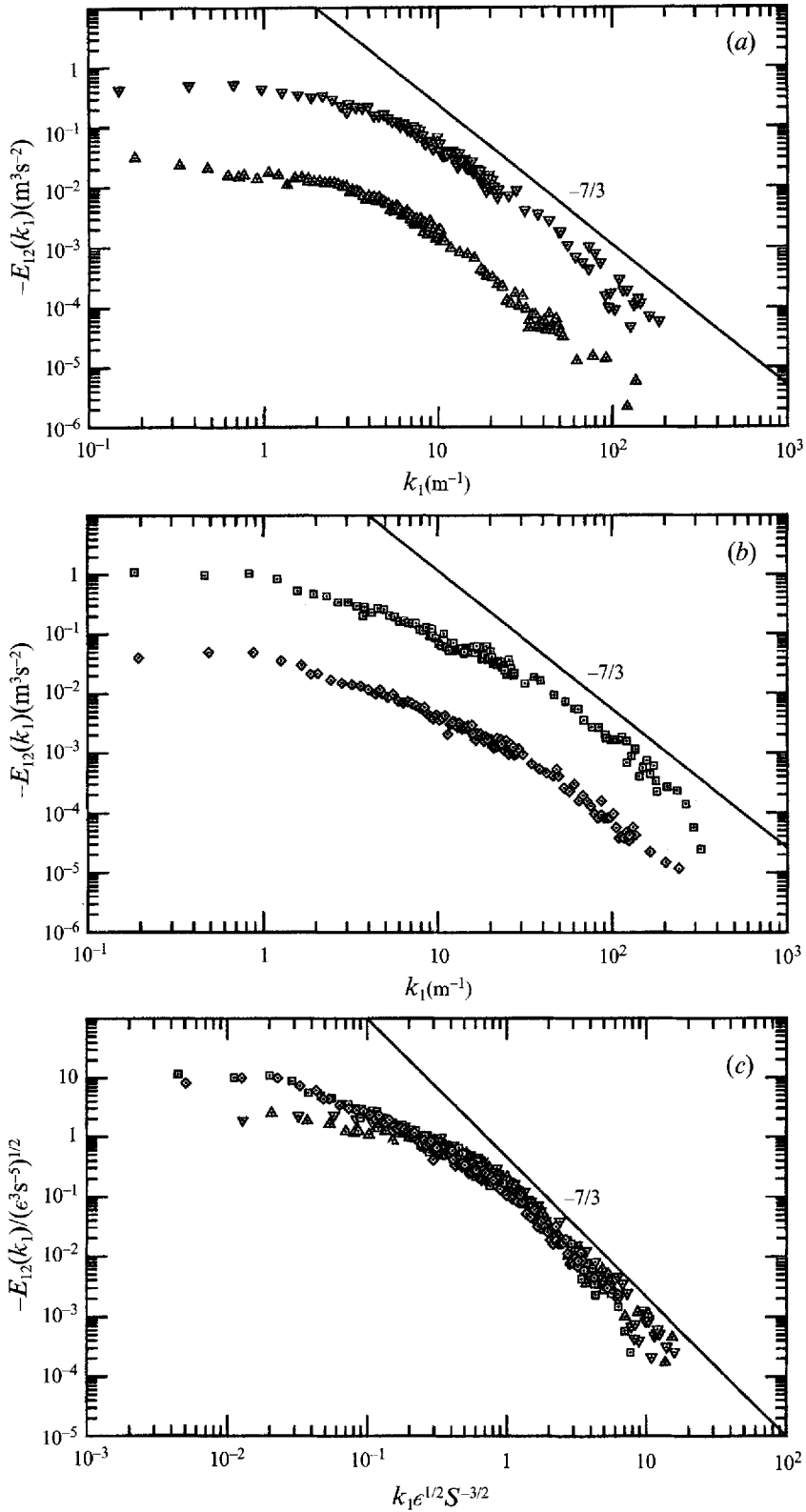


FIGURE 19. Shear-stress cospectra measured at different locations in the boundary layer for two different free-stream velocities. (a) Mid-layer; (b) inner-layer; (c) non-dimensional plot of (a) and (b) using  $(e/S^3)^{1/2}$  and  $(e/S)^{1/2}$  as length and velocity scales respectively.  $\nabla$ ,  $y = 400$  mm,  $R_\lambda \approx 1450$  (mid-layer, high-speed);  $\triangle$ ,  $y = 515$  mm,  $R_\lambda \approx 600$  (mid-layer, low-speed);  $\square$ ,  $y = 100$  mm,  $R_\lambda \approx 1400$  (inner-layer, high-speed);  $\diamond$ ,  $y = 100$  mm,  $R_\lambda \approx 500$  (inner-layer, low-speed).

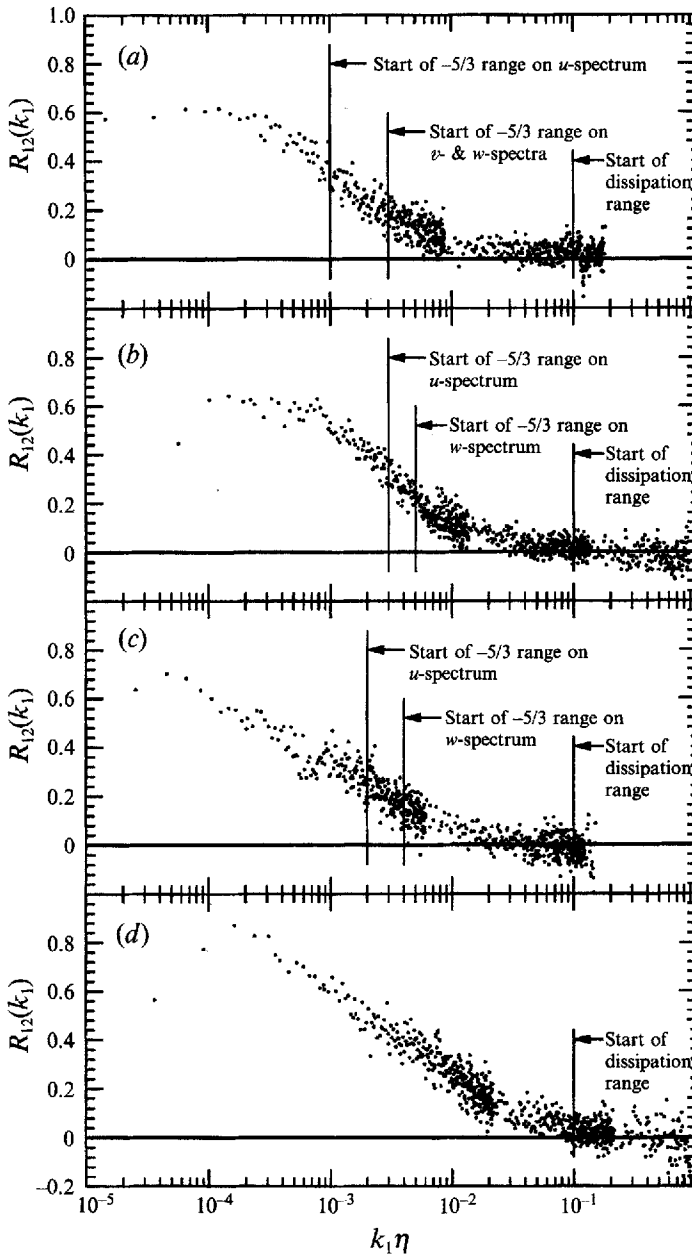


FIGURE 20. Correlation-coefficient spectra obtained at different locations in the boundary layer for two different free-stream velocities. (a)  $y = 400$  mm,  $R_\lambda \approx 1450$  (mid-layer, high-speed); (b)  $y = 515$  mm,  $R_\lambda \approx 600$  (mid-layer, low-speed); (c)  $y = 100$  mm,  $R_\lambda \approx 1400$  (inner-layer, high-speed); (d)  $y = 100$  mm,  $R_\lambda \approx 500$  (inner-layer, low-speed).

that both  $u_1$ - and  $u_2$ -spectra have  $-\frac{5}{3}$  ranges and the cospectrum exhibits a  $-\frac{7}{3}$  power law, then the correlation-coefficient spectrum should decay towards isotropy as  $k_1^{-\frac{5}{3}}$ . Based on their dynamical model, Nelkin & Nakano (1983) suggested that the decay of anisotropy should be no more rapid than  $k_1^{-\frac{5}{3}}$ , but could be slower.

Log-linear plots of the  $R_{12}(k_1)$  spectra are shown in figure 20. Each part of this figure contains data for one location in the boundary layer at one free-stream velocity. As mentioned earlier, both positive and negative values are inferred from the

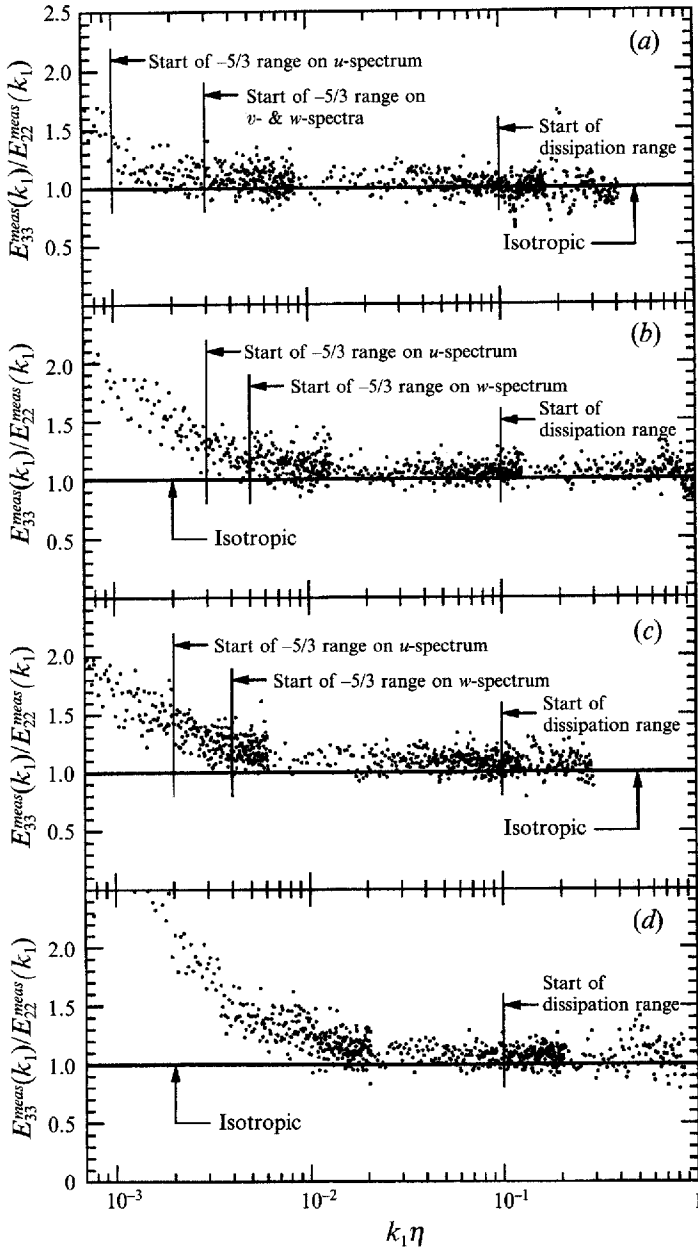


FIGURE 21. Ratios of the measured  $u_3$ -spectra to  $u_2$ -spectra at different locations in the boundary layer for two different free-stream velocities. For key to captions for (a)–(d) see figure 20.

measurements in the high-wavenumber ranges for all the measurement stations. This has been also observed in previous experiments by Champagne, Harris & Corrsin (1970), Antonia *et al.* (1992) and Henbest, Li & Perry (1992). While Champagne *et al.* attributed this to hot-wire spatial resolution problems and differences between the phase shifts of the two channels, Antonia *et al.*, who also noticed this phenomenon in a direct numerical simulation of turbulent channel flow, suggested that the positive values of  $E_{12}(k_1)$  corresponded to negative production of turbulent energy in the high-wavenumber range. However, based on their model for Taylor-hypothesis correction, Wyngaard & Clifford (1977) suggested that the convection velocity fluctuations would

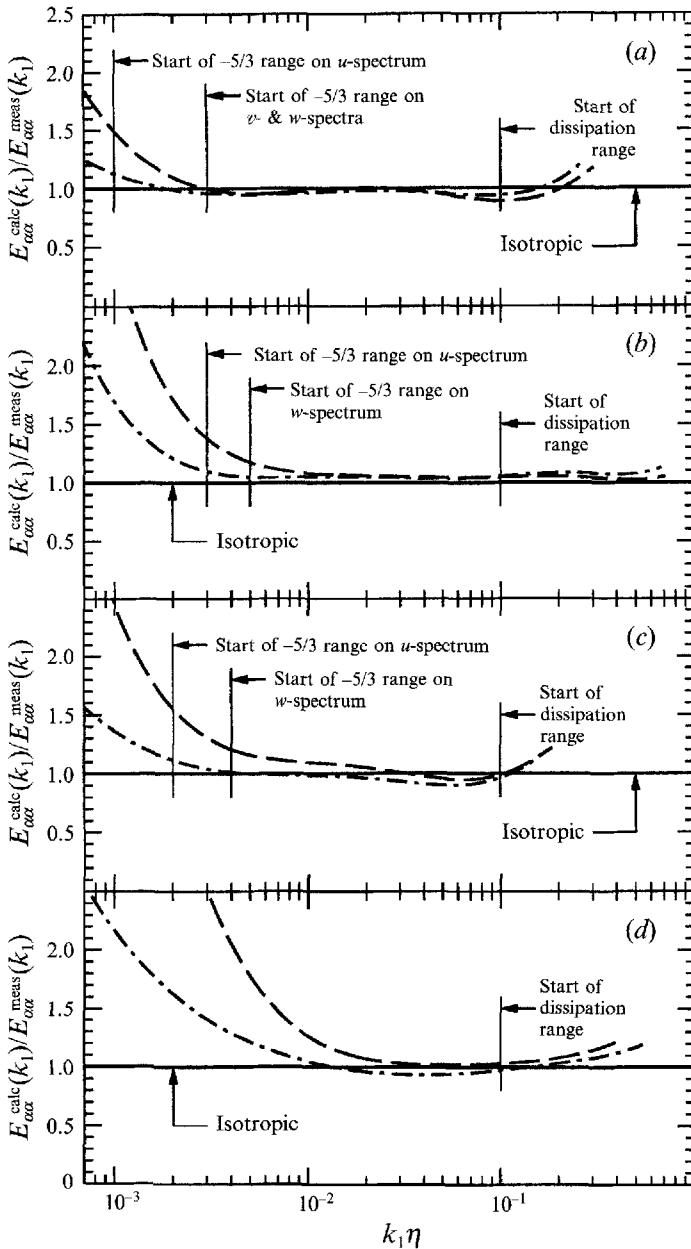


FIGURE 22. Ratios of the calculated to measured transverse spectra at different locations in the boundary layer for two different free-stream velocities. — — —,  $\alpha = 2$ ; - · - · -,  $\alpha = 3$ . For key to captions for (a)–(d) see figure 20.

alias enough spectral content into the measured cospectrum to make it appear to change sign at large  $k_1$ . For the present measurements, data for all channels were sampled simultaneously at sampling rates four times the low-pass filter cut-off frequencies, and there was a very good spatial resolution for the dissipation range at the mid-layer position for the low-speed case up to  $k_1\eta \leq 0.8$ . Figure 20 indicates that in the dissipation range ( $k_1\eta > 0.1$ ) at both the mid-layer (see also figure 11) and the inner-layer positions, local isotropy is satisfied, since (average)  $R_{12}(k_1) \approx 0$ .



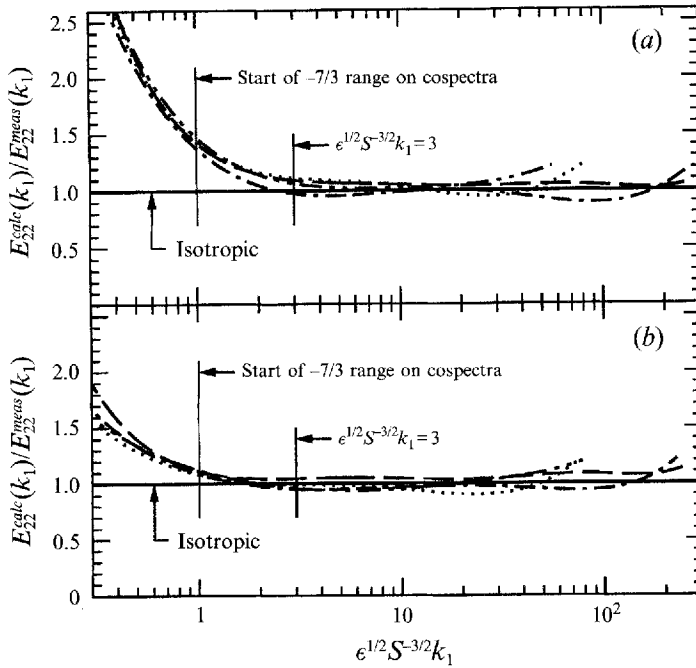


FIGURE 23. Scaling of the anisotropy ratios (figure 22) using the lengthscale  $(\epsilon/S^3)^{1/2}$ . (a)  $u_2$ -ratio; (b)  $u_3$ -ratio. —,  $y = 400$  mm,  $R_\lambda \approx 1450$  (mid-layer, high-speed); ---,  $y = 515$  mm,  $R_\lambda \approx 600$  (mid-layer, low-speed); ·····,  $y = 100$  mm,  $R_\lambda \approx 1400$  (inner-layer, high-speed); —·—·,  $y = 100$  mm,  $R_\lambda \approx 500$  (inner-layer, low-speed).

In the low-wavenumber range the correlation-coefficient spectra start their roll-off before the beginning of the  $-\frac{5}{3}$  ranges of longitudinal and transverse spectra. Figure 20(a) suggests that only in the range  $3 \times 10^{-3} < k_1 \eta < 10^{-2}$  does the correlation-coefficient spectra decay as  $k_1^{-\frac{2}{3}}$ , since only for  $k_1 \eta > 3 \times 10^{-3}$  do the  $u_1$ - and  $u_2$ -spectra, and the shear-stress cospectra simultaneously exhibit the expected inertial-subrange power laws. However, for  $k_1 \eta > 10^{-2}$ , there is still about one decade of  $R_{12}(k_1) \approx 0$ , before the start of the dissipation range.

The ratio of the measured  $u_3$ -spectrum to  $u_2$ -spectrum,  $E_{33}^{meas}(k_1)/E_{22}^{meas}(k_1)$ , should be unity, if the turbulence is isotropic. These ratios are shown in figure 21 for  $7 \times 10^{-4} \leq k_1 \eta \leq 1$ , which covers the entire inertial and dissipation ranges. It appears that, to within the accuracy of measurement, for the mid-layer high-speed case (figure 21 a), the  $u_3$ -spectrum becomes equal to  $u_2$ -spectrum at a higher wavenumber than the start of the  $-\frac{5}{3}$  range of the transverse spectra. However, for the other measurement locations, this occurs somewhat below the start of the spectral bumps.

The transverse spectra,  $E_{22}^{calc}(k_1)$  and  $E_{33}^{calc}(k_1)$ , can be calculated from the measured longitudinal spectrum,  $E_{11}^{meas}(k_1)$ , using (4). An anisotropy measure may be defined as  $E_{\alpha\alpha}^{calc}(k_1)/E_{\alpha\alpha}^{meas}(k_1)$ , where  $\alpha = 2$  or 3 corresponds to  $u_2$  or  $u_3$  respectively. These anisotropy measures should be equal to 1.0 in an isotropic flow. We have used the least-squares fit data in figures 12, 13, 14 and 15 to calculate these measures, which are shown in figure 22. For the inertial ranges, the trend in figure 22 almost matches figure 21. It appears that (4) can predict (to  $\pm 10\%$ ) the transverse spectra from the measured longitudinal spectrum for the entire inertial subrange of the transverse spectra. For the low-speed mid-layer position (figure 22 b), which had the best hot-wire spatial resolution, the isotropic value (to  $\pm 10\%$ ) is obtained for the dissipation range as well.

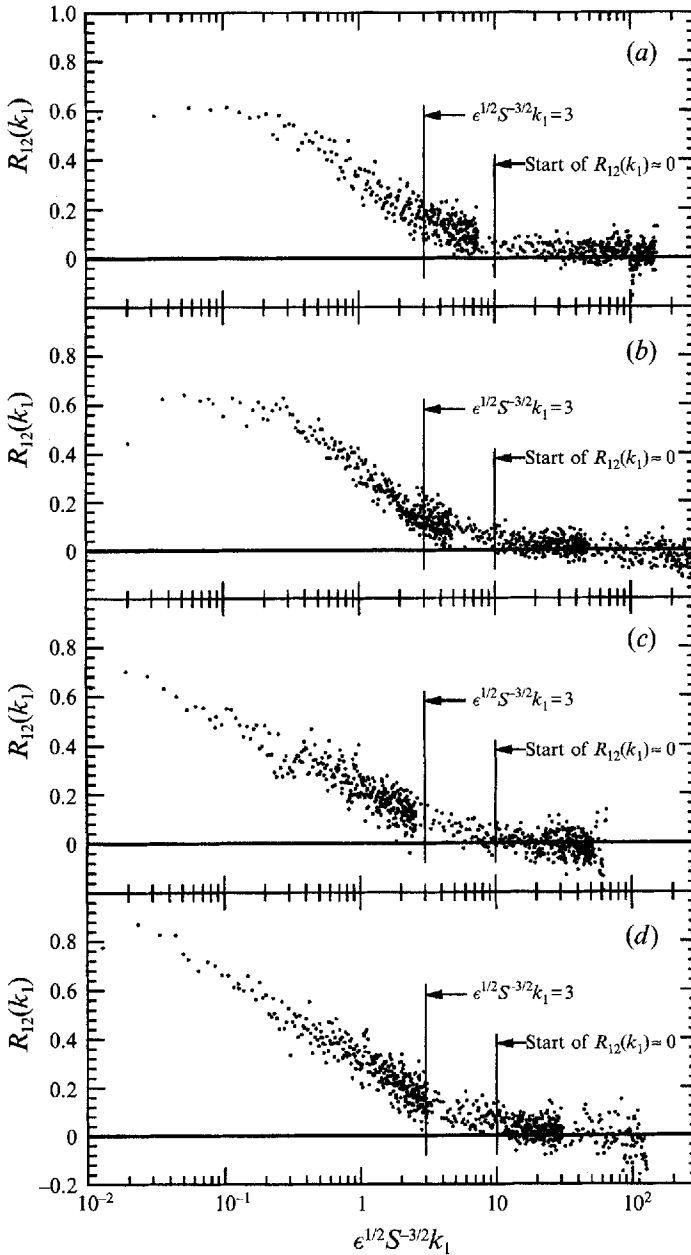


FIGURE 24. Scaling of the correlation-coefficient spectra (figure 20) using the lengthscale  $(\epsilon/S^3)^{1/2}$ .

Recall from table 1 that the spatial resolution in figure 22 varies from best to worst in the order: (b), (d), (a) and (c). Comparison of part (b) with the other three parts suggests that for the latter three cases, the deviations from the isotropic value at the high-wavenumber ends are not real, but rather are due to lack of spatial resolution.

Figure 22 suggests that as the wall is approached and the mean shear is increased, the anisotropy penetrates towards higher  $k_1 \eta$ . Therefore, a lengthscale that contains the effects of mean shear should collapse these ratios at the low-wavenumber end better than the Kolmogorov lengthscale  $\eta$ . The data plotted in figure 22 are scaled using the

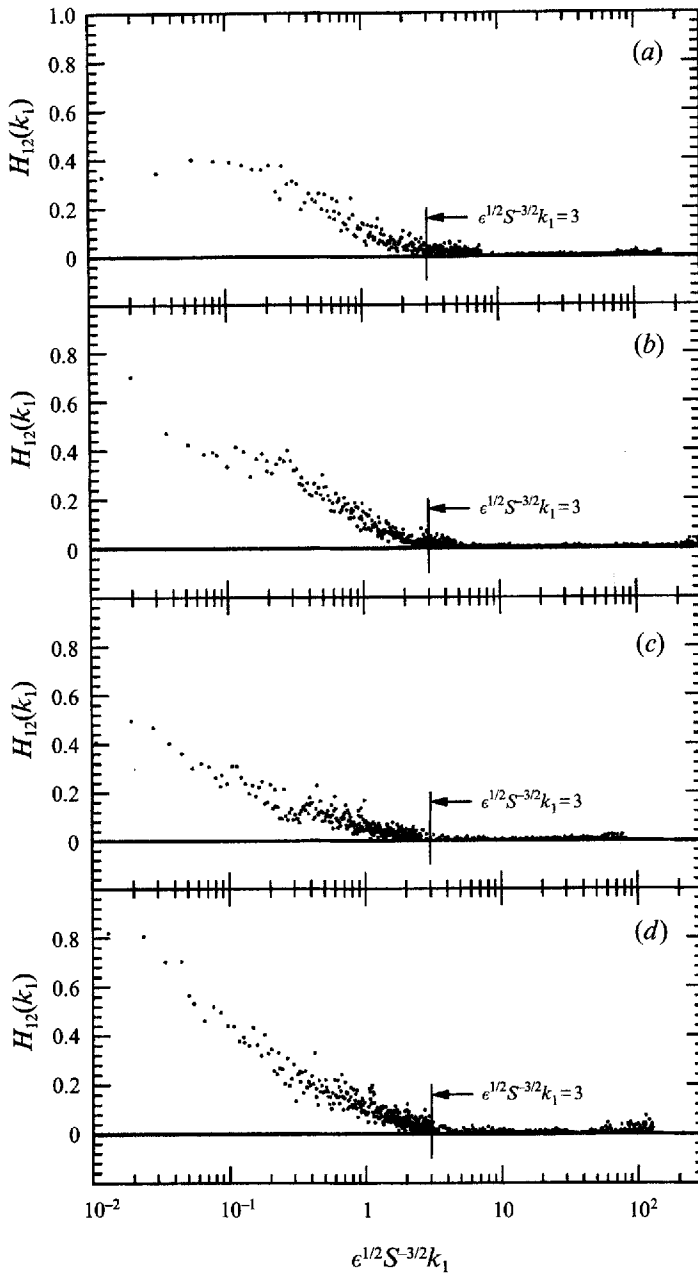


FIGURE 25. Spectral coherency measured at different locations in the boundary layer for two different free-stream velocities as a function of non-dimensional wavenumber  $k_1(\epsilon/S^3)^{\frac{1}{2}}$ . For key to captions for (a)–(d) see figure 20.

lengthscale  $(\epsilon/S^3)^{\frac{1}{2}}$  obtained from (29) and are shown in figure 23. A good collapse is obtained and it appears that, once the Corrsin–Uberoi condition ( $S_c^* \ll 1$ ) for the timescales is satisfied, local isotropy – as defined by (4) – is achieved in the inertial subrange for non-dimensional wavenumbers  $k_1(\epsilon/S^3)^{\frac{1}{2}} > 3$ . This is larger than the wavenumber ( $k_1(\epsilon/S^3)^{\frac{1}{2}} \approx 1$ ) for which the  $-\frac{7}{3}$  range begins in the shear-stress cospectra. The  $R_{12}(k_1)$  data, which were shown in figure 20, are plotted versus  $k_1(\epsilon/S^3)^{\frac{1}{2}}$

in figure 24. It appears that in the inertial subrange strict local isotropy,  $R_{12}(k_1) \approx 0$  and the isotropic relations among component spectra, is satisfied only for wavenumbers  $k_1(\epsilon/S^3)^{\frac{1}{2}} > 10$ : for the high-speed mid-layer position this corresponds to  $k_1 \eta > 0.01$ , which leaves about one decade of isotropic inertial subrange at this Reynolds number.

The spectral coherencies defined by (11) are shown in figure 25. They reach the isotropic value,  $H_{12}(k_1) \approx 0$ , sooner than the correlation-coefficient spectra, but at about the same non-dimensional wavenumber as the energy spectra (figure 23).

#### 4. General discussion and concluding remarks

The local-isotropy hypothesis (Kolmogorov 1941) – independence of small-scale structures from large-scale structures and mean deformations at high Reynolds numbers – has been used extensively in most approaches for studying turbulent flows, but its range of validity has been a subject of controversy. Of the two methods generally employed to investigate the properties of the small scales – direct numerical simulations and experiments – the latter was chosen for the current study, since present-day DNS cannot satisfy the high-Reynolds-number requirement which is an intrinsic part of the hypothesis. To over-come the resolution limitations of the instruments, high Reynolds numbers were achieved under controlled conditions in the 80 × 120 foot Full-Scale Aerodynamics Facility at NASA Ames Research Center. At one streamwise location and for free-stream velocities of 10 and 50 m s<sup>-1</sup>, extensive hot-wire measurements of the three components of velocity were made in the inner and outer layers of the test-section-ceiling rough-wall boundary layer. Acquisition of reliable data for the small-scale eddies was of prime concern. At this measurement location, the boundary-layer thickness was about 1 m and, at best, the smallest lengthscale resolved was about 1.5η. The maximum Reynolds numbers based on momentum thickness and on Taylor microscale were approximately 370 000 and 1450 respectively, the largest ever attained in laboratory boundary layers. By comparing the measured mean-velocity and Reynolds-stress profiles with other known data (Perry & Li 1990; Morrison *et al.* 1992), it was shown that the large-scale characteristics in the outer part of the boundary layer followed the standard behaviour.

The main aim of the present investigation was to study the effects of a simple mean-strain rate ( $S = \partial U / \partial y$ ) on local isotropy. The parameter characterizing these effects was identified (Corrsin 1958; Uberoi 1957) to be  $S_c^* (\equiv S(\nu/\epsilon)^{\frac{1}{2}})$ , which is the ratio of Kolmogorov and mean-shear timescales. Note that for a shear layer with (shear) production of turbulent kinetic energy approximately equal to dissipation,  $S_c^* \sim (R_\lambda)^{-1}$  approximately. The Corrsin–Uberoi condition,  $S_c^* \ll 1$ , for the existence of local isotropy in the ‘mixed range’ of spectra (the wavenumber range where both inertial transfer and viscous dissipation are important and where most of the dissipation occurs) was satisfied at all the measurement locations in the boundary layer at the Reynolds numbers under consideration. Expressions given by Wyngaard & Clifford (1977), based on the work of Lumley (1965), were used to estimate the errors arising from the use of Taylor’s hypothesis. For the wavenumbers of interest these errors were very small and no correction was applied to any of the present data.

To obtain the dissipation values, the compensated spectra were first analysed in the dissipation range. It was observed that in the dissipation range, spectra had a simple exponential decay (Kraichnan 1959) and that the exponent prefactor  $\beta = 5.2$  obtained in low-Reynolds-number direct-numerical-simulations (e.g. Kida *et al.* 1992) agrees reasonably well with the present data for  $0.5 \leq k_1 \eta \leq 1$ . The exponential form for the  $u_1$ -spectrum in the far-dissipation range was also observed in experiments by

Sreenivasan (1985) who proposed  $\beta = 8.8$  for  $0.5 \leq k_1 \eta \leq 1.5$  and by Chen *et al.* (1993) in numerical simulations who proposed  $\beta = 7.1$  for  $5 \leq k\eta \leq 10$ . The  $u_1$ -spectrum was compared with the data of Comte-Bellot & Corrsin (1971) for isotropic grid turbulence at  $R_\lambda = 60.7$ . In the dissipation range for  $0.1 < k_1 \eta < 0.5$  the agreement between the two  $u_1$ -spectra was good, but they deviated for  $k_1 \eta > 0.5$ .

Plots of compensated spectra proved to be a very sensitive test in the inertial subrange. The Kolmogorov constants obtained from the one-dimensional data at high Reynolds numbers satisfied the isotropic relations for the spectra and the second-order structure functions, and the constant for the three-dimensional spectrum,  $C$ , was estimated to be equal to  $1.5 \pm 0.1$  (Monin & Yaglom 1975). Spectral 'bumps' between the  $-\frac{5}{3}$  inertial subrange and the dissipative range were observed on all the compensated spectra. These have been previously found by Mestayer (1982) for velocity spectra and have also arisen in theoretical predictions such as the Eddy-Damped Quasi-Normal Markovian (EDQNM) theory. The shear-stress cospectral density  $E_{12}(k_1)$ , rolled-off with a  $-\frac{7}{3}$  power law, before the start of local isotropy in the energy spectra, and scaled linearly with  $S$  (Lumley 1967). To within the accuracy of measurement, the shear-stress cospectra, which are the most sensitive indicator of local isotropy, fell to zero at a wavenumber about a decade *larger* than that at which the energy spectra first followed  $-\frac{5}{3}$  power laws. At the highest Reynolds number  $E_{12}(k_1)$  fell to zero about one decade *before* the start of the dissipation range, and it remained zero in the dissipation range.

The lower wavenumber limit of locally isotropic behaviour of the shear-stress cospectra is given by  $k_1(\epsilon/S^3)^{\frac{1}{2}} \approx 10$ . The current investigation also indicates that for the energy spectra this limit may be relaxed to  $k_1(\epsilon/S^3)^{\frac{1}{2}} \approx 3$ : this is Corrsin's (1958) criterion, with the numerical value obtained from the present data. The existence of an *isotropic* inertial range requires that this wavenumber be much less than the wavenumber for the onset of viscous effects,  $k_1 \eta \ll 1$ , so that the combined condition (Corrsin 1958; Uberoi 1957), is  $S(\nu/\epsilon)^{\frac{1}{2}} \ll 1$ .

In summary, our results have confirmed the local-isotropy hypothesis and established the conditions under which local isotropy can be expected. It is shown that one decade of inertial subrange with truly negligible shear-stress cospectral density requires  $S_c^* \equiv S(\nu/\epsilon)^{\frac{1}{2}}$  not more than about 0.01 (for a shear layer with production of turbulent kinetic energy approximately equal to dissipation, a microscale Reynolds number of about 1500). For practical purposes many of the results of the hypothesis may be relied on at somewhat lower Reynolds numbers.

The effects of extra mean strain rates on the large-scale structure of shear flows (Bradshaw 1973) have been investigated extensively. Presently, the unanswered question is: will the above criteria obtained for the existence of local isotropy hold for complex non-equilibrium flows? Experiments to address this question are now being planned for the 80 × 120 foot wind tunnel.

We wish to thank Dr Fredric Schmitz, Chief of the Full-Scale Aerodynamics Research Division at NASA Ames, for permitting us to use the facility, and Dr James Ross, Group Leader, Basic Experiments, who has been, and will be in charge of coordinating our tests in the 80 × 120 foot wind tunnel. Our experiments would have not been possible without their help and the efforts of all the staff at the facility.

Throughout the course of this work, we have had many valuable discussions with Professors P. Bradshaw, P. Moin, W. C. Reynolds, and Drs J. Kim, R. S. Rogallo, J. G. Marvin, P. A. Durbin and A. A. Praskovsky. We thank them for all their help and advice. We thank Professor W. K. George for spending one week with us, during the course of which we investigated our hot-wire anemometry problems. We would also

like to thank Dr J. H. Watmuff and Professor J. K. Eaton, with whom we consulted about these problems. Professor A. E. Perry advised us on different aspects of this project especially hot-wire anemometry, and we have greatly benefited from suggestions made by Professors R. A. Antonia, C. W. Van Atta, M. Nelkin and J. G. Brasseur. We thank them all for their advice. We are also grateful to Dr N. R. Panchapakesan, who helped us during the second phase of these experiments.

## REFERENCES

- ANTONIA, R. A. & KIM, J. 1992 Isotropy of small-scale turbulence. *Proc. Summer Program of the Center for Turbulence Research, Stanford*.
- ANTONIA, R. A., KIM, J. & BROWNE, L. W. B. 1991 Some characteristics of small-scale turbulence in a turbulent duct flow. *J. Fluid Mech.* **233**, 369–388.
- ANTONIA, R. A., TEITEL, M., KIM, J. & BROWNE, L. W. B. 1992 Low Reynolds number effects in a fully developed turbulent channel flow. *J. Fluid Mech.* **236**, 579–605.
- BATCHELOR, G. K. 1946 The theory of axisymmetric turbulence. *Proc. R. Soc. Lond. A* **186**, 480–502.
- BATCHELOR, G. K. 1953 *The Theory of Homogeneous Turbulence*. Cambridge University Press.
- BENDAT, J. S. & PIERSON, A. G. 1986 *Random Data Analysis and Measurement Procedures*. John Wiley & Sons.
- BRADSHAW, P. 1971 *An Introduction to Turbulence and its Measurement*. Pergamon.
- BRADSHAW, P. 1973 Effects of streamline curvature on turbulent flow. *AGARDograph* 169.
- BRASSEUR, J. G. 1991 Comments on the Kolmogorov hypothesis of isotropy in the small scales. *Paper AIAA-91-0230; 29th Aerospace Sciences Meeting, January 7–10, 1991, Reno, Nevada*.
- BROWNE, L. W. B., ANTONIA, R. A. & SHAH, D. A. 1987 Turbulent energy dissipation in a wake. *J. Fluid Mech.* **179**, 307–326.
- CAUGHEY, S. J., WYNGAARD, J. C. & KAIMAL, J. C. 1979 Turbulence in the evolving stable boundary layer. *J. Atmos. Sci.* **36**, 1041–1052.
- CHAMPAGNE, F. H. 1978 The fine-scale structure of the turbulent velocity field. *J. Fluid Mech.* **86**, 67–108.
- CHAMPAGNE, F. H., FRIEHE, C. A., LA RUE, J. C. & WYNGAARD, J. C. 1977 Flux measurements, flux estimation techniques and fine scale turbulent measurements in the surface layer over land. *J. Atmos. Sci.* **34**, 515–530.
- CHAMPAGNE, F. H., HARRIS, V. G. & CORRSIN, S. 1970 Experiments on nearly homogeneous turbulent shear flow. *J. Fluid Mech.* **41**, 81–139.
- CHANDRASEKHAR, S. 1950 The theory of axisymmetric turbulence. *Proc. R. Soc. Lond. A* **242**, 557–577.
- CHAPMAN, D. 1979 Computational aerodynamics development and outlook. *AIAA J.* **17**, 1293–1313.
- CHEN, S., DOOLEN, G., HERRING, J. R., KRAICHNAN, R. H., ORSZAG, S. A. & ZHEN, S. S. 1993 Far dissipation range of turbulence. *Phys. Rev. Lett.* **70**, 3051.
- COANTIC, M. & FAVRE, A. 1974 Activities in, and preliminary results of, air-sea interactions research at I.M.S.T. *Adv. Geophys.* **18A**, 391–405.
- COMTE-BELLOT, G. & CORRSIN, S. 1971 Simple Eulerian time correlation of full and narrow-band velocity signals in grid-generated ‘isotropic’ turbulence. *J. Fluid Mech.* **48**, 273–337.
- CORRSIN, S. 1958 On local isotropy in turbulent shear flow. *NACA R & M* 58B11.
- DOMARADZKI, A. J. & ROGALLO, R. S. 1988 Energy transfer in isotropic turbulence at low Reynolds numbers. *Proc. Summer Program of the Center for Turbulence Research, CTR-S88*, pp. 169–177. Center for Turbulence Research, Stanford University/NASA Ames.
- DOMARADZKI, A. J., ROGALLO, R. S. & WRAY, A. A. 1990 Interscale energy transfer in numerically simulated homogeneous turbulence. *Proc. Summer Program of the Center for Turbulence Research, CTR-S90*, pp. 319–329. Center for Turbulence Research, Stanford University/NASA Ames.
- DURBIN, P. A. & SPEZIALE, C. G. 1991 Local anisotropy in strained turbulence at high Reynolds numbers. *Recent Advances in Mechanics of Structured Continua*, vol. 117, p. 29.

- EWING, D. W. & GEORGE, W. K. 1992 Spatial resolution of multi-wire probes. *45th Annual Meeting of the Fluid Dynamics Division of the American Physical Society, Tallahassee*, vol. 37, No. 8.
- GEORGE, W. K. & HUSSEIN, H. J. 1991 Locally axisymmetric turbulence. *J. Fluid Mech.* **233**, 1–23.
- GIBSON, M. M. 1963 Spectra of turbulence in a round jet. *J. Fluid Mech.* **15**, 161–173.
- GRANT, H. L. & MOILLIET, A. 1962 The spectrum of a cross-stream component of turbulence in a tidal stream. *J. Fluid Mech.* **13**, 237–240.
- GRANT, H. L., STEWART, R. W. & MOILLIET, A. 1962 Turbulence spectra from a tidal channel. *J. Fluid Mech.* **12**, 241–268.
- HENBEST, S. M., LI, J. D. & PERRY, A. E. 1992 Turbulence spectra in the near-wall region. *Proc. 11th Australasian Fluid Mech. Conf., Univ. of Tasmania, Australia*.
- HINZE, J. O. 1975 *Turbulence*. McGraw-Hill.
- HUNT, J. C. R., PHILLIPS, O. M. & WILLIAMS, D. 1991 Turbulence and stochastic processes: Kolmogorov's ideas 50 years on. *Proc. R. Soc. Lond. A* **434**.
- KARYAKIN, M. Y., KUZNETSOV, V. R. & PRASKOVSKY, A. A. 1991 *Izv. Akad. Nauk SSSR, Mech. Zhidk. i Gaza* **5**, 51–59.
- KERR, R. M. 1990 Velocity, scalar and transfer of spectra in numerical turbulence. *J. Fluid Mech.* **211**, 309–332.
- KIDA, S., KRAICHNAN, R. H., ROGALLO, R. S., WALEFFE, F. & ZHOU, Y. 1992 Triad interactions in the dissipation range. *Proc. Summer Program of the Center for Turbulence Research, CTR-S92*, pp. 83–99. Center for Turbulence Research, Stanford University/NASA Ames.
- KIDA, S. & MURAKAMI, Y. 1987 Kolmogorov similarity in freely decaying turbulence. *Phys. Fluids A* **30**, 2030–2039.
- KIM, J. & HUSSAIN, F. 1993 Propagation velocity of perturbations in turbulent channel flow. *Phys. Fluids A* **5**, 695–706.
- KISTLER, A. L. & VREBALOVICH, T. 1966 Grid turbulence at large Reynolds numbers. *J. Fluid Mech.* **26**, 37–47.
- KOLMOGOROV, A. N. 1941 The local structure of turbulence in incompressible viscous fluid for very large Reynolds numbers. *C. R. Acad. Sci URSS* **30**, 301.
- KOLMOGOROV, A. N. 1962 A refinement of previous hypotheses concerning the local structure of turbulence in a viscous incompressible fluid at high Reynolds number. *J. Fluid Mech.* **13**, 82–85.
- KRAICHNAN, R. H. 1959 The structure of isotropic turbulence at very high Reynolds numbers. *J. Fluid Mech.* **5**, 497–543.
- LANDAU, L. D. & LIFSHITZ, E. M. 1987 *Fluid Mechanics*. Pergamon.
- LAUFER, J. 1954 The structure of turbulence in fully developed pipe flow. *NACA Rep.* 1174.
- LEE, M. J., KIM, J. & MOIN, P. 1990 Structure of turbulence at high shear rate. *J. Fluid Mech.* **216**, 561–583.
- LIGRANI, P. M. & BRADSHAW, P. 1987 Spatial resolution and measurement of turbulence in the viscous sublayer using subminiature hot-wire probes. *Exps Fluids*, **5**, 407–417.
- LUMLEY, J. L. 1965 Interpretation of time spectra measured in high-intensity shear flows. *Phys. Fluids*, **8**, 1056–1062.
- LUMLEY, J. L. 1967 Similarity and the turbulent energy spectrum. *Phys. Fluids*, **10**, 855–858.
- MESTAYER, P. 1982 Local isotropy and anisotropy in a high-Reynolds-number turbulent boundary layer. *J. Fluid Mech.* **125**, 475–503.
- MESTAYER, P., CHOLLET, J. P. & LESIEUR, M. 1983 Inertial subrange of velocity and scalar variance spectra in high-Reynolds-number three-dimensional turbulence. In *Turbulence and Chaotic Phenomena in Fluids* (ed. T. Tatsumi), p. 285. Elsevier.
- MOIN, P. 1990 Similarity of organized structures in turbulent shear flows. In *Near-Wall Turbulence* (ed. S. J. Kline & N. H. Afgan), p. 2. Hemisphere.
- MONIN, A. S. & YAGLOM, A. M. 1975 *Statistical Fluid Mechanics*, Vol. 2. MIT Press.
- MORRISON, J. F., SUBRAMANIAN, C. S. & BRADSHAW, P. 1992 Bursts and the law of the wall in turbulent boundary layers. *J. Fluid Mech.* **241**, 75–108.
- NELKIN, M. & NAKANO, T. 1983 How do the small scales become isotropic in Navier–Stokes turbulence. In *Turbulence and Chaotic Phenomena in Fluids* (ed. T. Tatsumi), p. 319. Elsevier.
- ONSAGER, L. 1949 Statistical hydrodynamics. *Nuovo Cimento* **6**, suppl. 2, 279–287.

- PAO, Y. H. 1965 Structure of turbulent velocity and scalar fields at large wave numbers. *Phys. Fluids* **8**, 1063–1075.
- PERRY, A. E. 1982 *Hot-Wire Anemometry*. Clarendon.
- PERRY, A. E. & JOUBERT, P. N. 1963 Rough wall boundary layers in adverse pressure gradients. *J. Fluid Mech.* **17**, 193–211.
- PERRY, A. E. & LI, J. D. 1990 Experimental support for the attached-eddy hypothesis in zero-pressure-gradient turbulent boundary layers. *J. Fluid Mech.* **218**, 405–438.
- PIOMELLI, U., BALINT, J. L. & WALLACE, J. M. 1989 On the validity of Taylor's hypothesis for wall-bounded turbulent flows. *Phys. Fluids A* **1**, 609–611.
- POND, S., PHELPS, G. T., PAQUIN, J. E., MCBEAN, G. & STEWART, R. W. 1971 Measurements of the turbulent fluxes of momentum, moisture, and sensible heat over the ocean. *J. Atmos. Sci.* **28**, 901–917.
- SADDOUGHI, S. G. 1992 Local isotropy in high Reynolds number turbulent shear flows. *Annual Research Briefs of the Center for Turbulence Research*, pp. 237–262. Stanford University/NASA Ames.
- SANADA, T. 1992 Comment on the dissipation-range spectrum in turbulent flows. *Phys. Fluids A* **4**, 1086–1087.
- SANBORN, V. A. & MARSHALL, R. D. 1965 Local isotropy in wind tunnel turbulence. *Colorado State Univ. Rep.* CER 65 UAS-RDM71.
- SREENIVASAN, K. R. 1985 On the fine-scale intermittency of turbulence. *J. Fluid Mech.* **151**, 81–103.
- SREENIVASAN, K. R. 1991 On local isotropy of passive scalars in turbulent shear flows. *Proc. R. Soc. Lond A* **434**, 165–182.
- TAYLOR, G. I. 1935 Statistical theory of turbulence. *Proc. R. Soc. Lond. A* **151**, 421.
- TIELEMAN, H. W. 1967 Viscous region of turbulent boundary layer. *Colorado State Univ. Rep.* CER 67–68 HWT21.
- TOWNSEND, A. A. 1948 Local isotropy in the turbulent wake of a cylinder. *Austral. J. Sci. Res.* **2**, 161–174.
- TOWNSEND, A. A. 1976 *The Structure of Turbulent Shear Flow*, 2nd edn. Cambridge University Press.
- UBEROI, M. S. 1957 Equipartition of energy and local isotropy in turbulent flows. *J. Appl. Phys.* **28**, 1165–1170.
- UBEROI, M. S. & FREYMUTH, P. 1969 Spectra of turbulence in wakes behind circular cylinders. *Phys. Fluids A* **12**, 1359–1363.
- VAN ATTA, C. 1991 Local isotropy of the smallest scales of turbulent scalar and velocity fields. *Proc. R. Soc. Lond. A* **434**, 139–147.
- VEERAVALLI, S. V. & SADDOUGHI, S. G. 1991 A preliminary experimental investigation of local isotropy in high-Reynolds-number turbulence. *Annual Research Briefs of the Center for Turbulence Research*, pp. 3–20. Stanford University/NASA Ames.
- WALEFFE, F. 1991 The nature of triad interactions in homogeneous turbulence. *Phys. Fluids A* **4**, 350–363.
- WILLIAMS, R. N. & PAULSON, C. A. 1978 Microscale temperature and velocity spectra in the atmospheric boundary layer. *J. Fluid Mech.* **83**, 547–567.
- WYNGAARD, J. C. 1968 Measurements of small-scale turbulence structure with hot wires. *J. Sci. Instrum.* **1**, 1105–1108.
- WYNGAARD, J. C. & CLIFFORD, S. F. 1977 Taylor's hypothesis and high-frequency turbulence spectra. *J. Atmos. Sci.* **34**, 922–929.
- WYNGAARD, J. C. & COTE, O. R. 1972 Co-spectral similarity in the atmospheric surface layer. *Q. J. R. Met. Soc.* **98**, 590–603.
- YEUNG, P. K. & BRASSEUR, J. G. 1991 The response of isotropic turbulence to isotropic and anisotropic forcing at the large scales. *Phys. Fluids A* **3**, 884–897.